Geological Quarterly, 2023, 67: 2
DOI: http://dx.doi.org/10.7306/gq.1673

Insights into the palaeoenvironments, structure and stratigraphy of the lower Miocene of the Eastern Carpathians Bend Zone, Romania

Răzvan-Ionuţ BERCEA[1, 2], Ramona BĂLC[3, 4, *], Alexandra TĂMAŞ[1], Sorin FILIPESCU[1], Dan Mircea TĂMAŞ[1], Marcel GUILLONG[5], Szabolcs Flavius SZEKELY[1] and Réka LUKÁCS[6, 7]

1 Babeş-Bolyai University, Department of Geology and Research Center for Integrated Geological Studies, 1 Kogălniceanu Street, 400084 Cluj-Napoca, Romania; ORCID: 0000-0002-0438-7770 [R.-I.B.], 0000-0001-8010-1853 [A.T.], 0000-0002-6640-8928 [D.M.T.], 0000-0002-6792-9776 [S.F.], 0000-0001-8639-8512 [S.F.S]

2 S.N.G.N. Romgaz S.A. Tîrgu-Mureş, 23 Salcâmilor Street, Romania; ORCID: 0000-0002-0438-7770 [R.-I.B.]

3 Babeş-Bolyai University, Faculty of Environmental Science and Engineering, 30 Fântânele Street, 400294 Cluj-Napoca, Romania; ORCID: 0000-0002-9419-2351 [R.B.]

4 Babeş-Bolyai University, Interdisciplinary Research Institute on Bio-Nano-Sciences, 42 Treboniu Laurian Street, 400271 Cluj-Napoca, Romania; ORCID: 0000-0002-9419-2351 [R.B.]

5 Institute of Geochemistry and Petrology, Department of Earth Sciences, ETH Zürich, Clausius Strasse 25, 8092 Zürich, Switzerland; ORCID: 0000-0002-6920-3362 [M.G.]

6 Institute for Geological and Geochemical Research, Research Centre for Astronomy and Earth Sciences [MTA Centre of Excellence], Eötvös Loránd Research Network (ELKH), Budaörsi út 45, 1112 Budapest, Hungary; ORCID: 0000-0002-2338-4209 [R.L.]

7 MTA-ELTE Volcanology Research Group, Eötvös Loránd Research Network (ELKH), Pázmány P. sétány 1/C, 1117 Budapest, Hungary; ORCID: 0000-0002-2338-4209 [R.L.]

Bercea, R.I., Bălc, R., Tămaş, A., Filipescu, S., Tămaş, D.M., Guillong, M., Szekely, S.F., Lukács, R., 2023. Insights into the palaeoenvironments, structure and stratigraphy of the lower Miocene of the Eastern Carpathians Bend Zone, Romania. Geological Quarterly, 67: 2, doi: 10.7306/gq.1673

The ages of several Oligocene to Miocene sedimentary formations from the Eastern Carpathians Bend Zone are poorly constrained due to palaeoenvironmental factors, reworking of fossils, structural complexity and limited exposure. To help overcome these issues, this study integrates calcareous nannoplankton and foraminifera biostratigraphy with isotopic age dating (U-Pb) of volcaniclastic zircons, and sedimentological and structural observations/interpretations. Our study was carried out along an ~6-km-long section made from a series of outcrops along the Bizdidel River which exposes several formations such as the Pucioasa, Fusaru, Vineţişu, Starchiojd and Slon. We show that the Fusaru Formation consists of coarse-grained rocks deposited as confined longitudinal channel successions that migrated laterally. It is bounded by the mud-rich Pucioasa and Vineţişu formations which are lateral equivalents of the Fusaru confined channels deposited as levee/overbank units. These genetically related formations appear to reach younger ages – of the lower to middle Burdigalian based on calcareous nannoplankton and foraminifera biostratigraphy – than previously thought (upper Oligocene to lower Burdigalian). The dominant organic-rich mudstones of the Starchiojd Formation represent pelagites/hemipelagites deposited in anoxic conditions. Their middle Burdigalian age is established by a 17.41 ±0.27 Ma zircon U-Pb age of zircons from the Bătrâni Tuff in the Starchiojd Formation. Based on the similar phenocryst content, zircon U-Pb age and zircon trace element composition, the source of the tuff is suggested to be the 17.3 Ma Eger ignimbrite-forming eruption, which has proximal, near-caldera deposits in the Bükkalja Volcanic Field, Hungary. The mud-rich Slon Formation seems to be related to shelf edge/upslope failure that formed cohesive debrite avalanches resulting from foreland propagation of compression. The Slon Formation extends in this area to at least the upper part of the lower Miocene to middle Miocene. These results highlight the need to revise ages of those parts of the sequence which are poorly constrained or different in other parts of the Carpathian Basin. Such revised ages help to better constrain the understanding of the deformation history of the Carpathians.

Key words: biostratigraphy, tuff, zircon U-Pb age, sedimentology, structural geology.

* Corresponding author, e-mail: ramona.balc@ubbcluj.ro

Received: August 11, 2022; accepted: December 21, 2022; first published online: January 31, 2023

INTRODUCTION

The specific tectonic and palaeoenvironmental conditions operating during the Oligocene to Miocene in the Eastern Carpathians Bend Zone (ECBZ; Fig. 1) has led to limitations in assigning the relative ages of several formations. Traditionally considered Oligocene to lower Miocene (Mărunţeanu, 1999; Melinte and Brustur, 2008; Melinte and Stoica, 2013), recent studies carried out in the ECBZ revealed that at least locally some formations may be younger, up to the middle Miocene; Tămaş, 2018; Filipescu et al., 2020).

One problem in this area is the extensive reworking (Szabo, 2012), hence the traditional biostratigraphy rarely provides reliable markers. However, locally, calcareous nannoplankton and foraminifera may give useful biostratigraphic clues, especially when long sections are available.

More reliable stratigraphic data and information may be obtained by combining the biostratigraphy and sedimentology with radioisotopic data, all analysed in a structural context. Also, by doing this, some lithostratigraphic units can be re-interpreted as contemporaneous equivalents, rather than as successive units.

The presence of a ~6 kilometres long mildly deformed section at Pucioasa, along the Bizdidel Valley (Fig. 2A), where several formations crop out (Pucioasa, Fusaru, Vineţişu, Starchiojd and Slon; Fig. 3) created the opportunity for a re-interpretation of the stratigraphy and depositional environments. Moreover, the occurrence of a volcanic tuff intercalation (Bătrâni Tuff, Ştefănescu et al., 1993) in a regionally developed unit (Starchiojd Formation) proved to be of great help for stratigraphic calibration, by using zircon U-Pb age dating. The source area for the tuff based on petrology, zircon age dating and trace element composition is also discussed.

Our results, including more precise formation ages and a revised depositional environment for the Miocene deep marine formations, will better help to constrain the stratigraphy, tectonic deformation and palaeoenvironments of the Carpathians.

GEOLOGICAL SETTING

STRUCTURAL OVERVIEW

The Carpathians have a highly arcuate orogen shape (Fig. 1A) due to their palaeogeographic evolution in relation to the European/Moesian platforms, and Tisza, Dacia and Alcapa continental megablocks (Schmidt et al., 2008).

Following an extensional phase between the Triassic and early Cretaceous (Săndulescu, 1984, 1988), the tectonic history of the Carpathians is characterized by subsequent compressional deformation (Săndulescu, 1988; Hippolyte and Săndulescu, 1996; Maţenco and Bertotti, 2000; Leveer et al., 2006).

The overall thrusting implies a foreland propagating sequence (Maţenco and Bertotti, 2000) that formed a general eastwards (i.e. Eastern Carpathians) and southwards (i.e. South Carpathians) verging nappe system (Schmidt et al., 2008). The ECBZ (Fig. 1B) represents the transition between these two systems (Leveer et al., 2006). Based on the age and style of deformation (thin vs. thick-skinned; Săndulescu, 1984), different nappes have been described (see Săndulescu, 1984; 1988; Fig. 1C). The thick-skinned nappes consist of pre-Alpine basement rocks, metamorphosed during the Paleozoic (Kraütner and Bindea, 2002; Medaris et al., 2003; Balintoni et al., 2014; Ducea et al., 2016) and Cretaceous sedimentary/magmatic formations thrusted during the Early and Late Cretaceous (Săndulescu, 1984; Fig. 1B, C). The Cretaceous to middle Miocene sequence among the thin-skinned nappes thrusted during the late Paleogene to middle Miocene (Săndulescu, 1988; Răbăgia et al., 2011; Fig. 1B, C). The Tarcău Nappe, which represents the subject of our study, was considered to be emplaced from the early Miocene, with an intra-Burdigalian onset (Săndulescu 1984; Merten et al., 2010) or probably even later (middle Miocene; Filipescu et al., 2020). Also, Schleder et al., (2019) suggested that some folding/thrusting and erosion took place during the intra-Burdigalian phase in the proximal part of the Tarcău Nappe (Fig. 1D). The compression continued towards the foreland (Maţenco and Bertotti, 2000; Merten et al., 2010) mostly in a piggyback setting (e.g., Valea Lungă Syncline, Fig. 1D; Bercea et al., 2016; Tămaş, 2018; Schleder et al., 2019). The latest deformation (the Wallachian phase – Meotian to Recent; Hippolyte and Săndulescu, 1996) that affected the ECBZ was related to crustal-scale shortening through the reactivation of basement faults and produced uplift/erosion of 4–5 km (Sanders et al., 1999; Merten et al., 2010). This phase was characterized by minor deformation under N–S compression. The Wallachian structures are represented by gentle to open folds (Hippolyte and Săndulescu, 1996; Schleder et al., 2019).

STRATIGRAPHY AND PRE-EXISTING AGE CONSTRAIN

The Tarcău Nappe consists of Cretaceous to middle Miocene formations. Two different lithofacies have been defined for the deep marine Oligocene to lower Miocene deposits of the Tarcău Nappe of the ECBZ (Conţescu et al., 1966; Sylvester and Lowe, 2004; Răbăgia et al., 2011; Szabo 2012): an internal one, of Carpathian origin, of Pucioasa-Fusaru facies, and an external one, of foreland origin (non-Carpathian), with a bituminous facies and Kliwa-type sandstones (Săndulescu et al., 1995); an interbedded zone exists between the two lithofacies (Pătruţ, 1955).

The lower Oligocene started in the ECBZ with the deposition of dark-coloured organic-rich shales/bituminous menilites of the “lower dysodiles”/“menilites” (Olteanu, 1952; Popescu, 1952; Melinte and Brustur, 2008). The Pucioasa and Fusaru formations (Mrazec and Popescu-Voiteşti, 1914; Olteanu, 1952; Pătruţ, 1955) were considered as late Oligocene (NP24-NP25) based on the presence of *Pontosphaera enormis*, *Triquetrorhabdulus carinatus*, *Sphenolithus conicus* and *S. delphix* calcareous nannoplankton (Vineţişu Valley – ECBZ; Melinte and Brustur, 2008). The Pucioasa-type deposits consist of dark grey massive/laminated calcareous mudstones, rare organic-rich mudstones (Pătruţ, 1955) with thin cross/planar-laminated very fine- to fine-grained sandstones and siltstones (Szabo, 2012; Frunzescu, 2013) as well as rare thin coccolithic limestones (Melinte and Brustur, 2008). The Fusaru deposits consist of subgreywacke, quartzo-feldspathic calcareous sandstones, conglomerates/breccias and mudstone intercalations. They are embedded in the Pucioasa Formation (Ştefănescu et al., 1988; Săndulescu et al., 1995; Sylvester and Lowe, 2004; Szabo, 2012). The Pucioasa facies was first described by Mrazec and Popescu-Voiteşti (1912 *fide* Pătruţ, 1955) and the Fusaru facies by Popescu-Voiteşti (1910 *fide* Ştefănescu, 1995) from around the town of Pucioasa. In the Eastern Carpathians, north of the area investigated, based on the presence of the foraminifer *Globoquadrina dehiscens* (Tarcuţa River, northern part of the Eastern Carpathians) in the mudstones of the Fusaru Formation, an age of not older than Aquitanian was assigned (Belayouni et al., 2007). A Fusaru-like

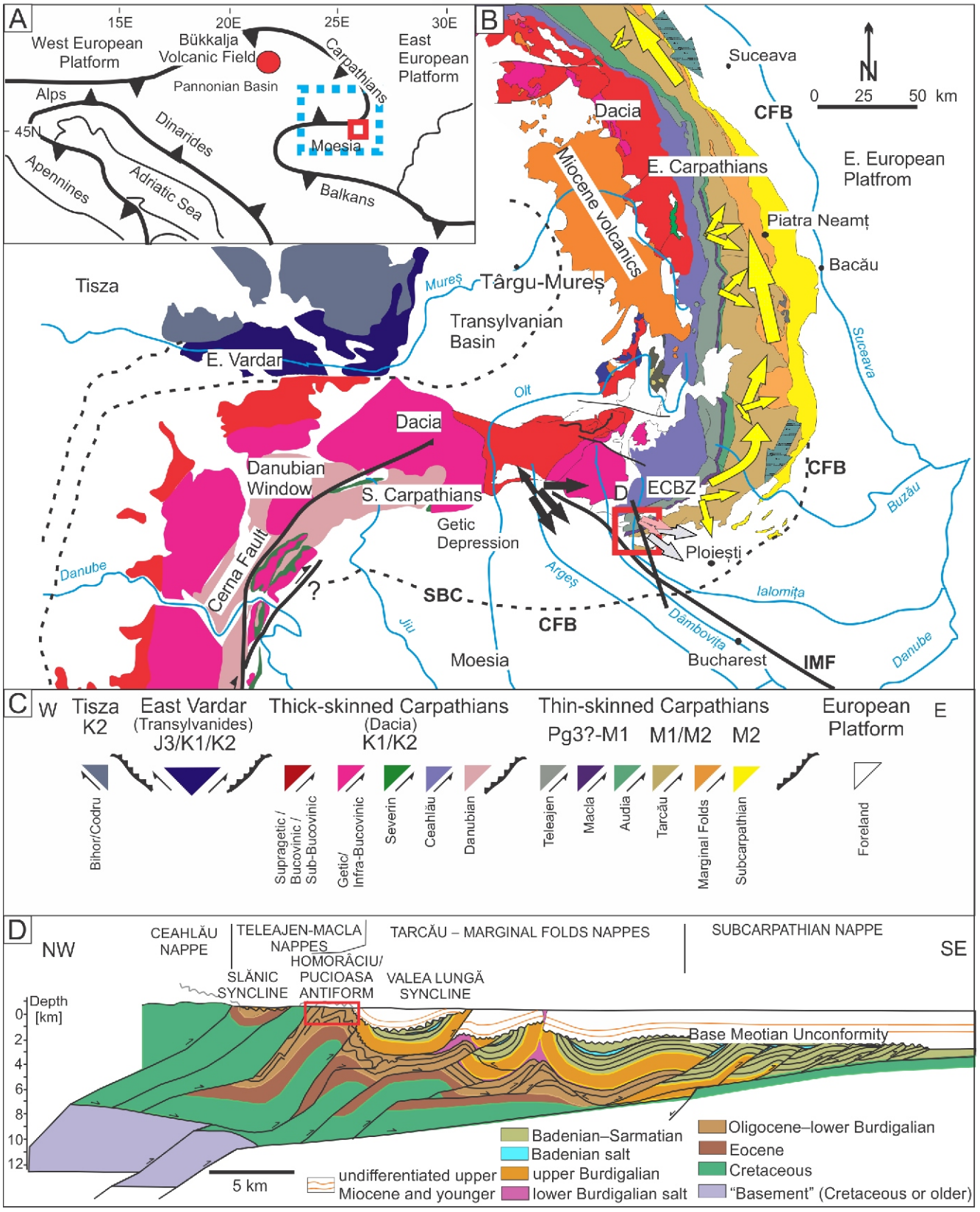

Fig. 1A – location of the Romanian Carpathians within the Alpine-Carpathian belt (Krézsek et al., 2013); red circle = Bükkalja Volcanic Field; dashed blue rectangle – Fig. 1B; red square – area of interest; B – tectonic sketch of the Romanian Carpathians (modified from Krézsek et al., 2013 based on Săndulescu, 1988; Bădescu, 2005; Schmid et al., 2008), red square – area of interest, arrows – palaeocurrent directions (p.d.) from different formations (Conţescu et al., 1966), black arrows – p.d. for the Corbi/Cheia formations (Jipa, 1982; 1994 *fide* Roban, 2008), pink arrows – p.d. from Fusaru deposits (this study), SBC – subsurface Subcarpathian Nappe, CFB – Carpathians Foredeep basin, IMF – IntraMoesian Fault, ECBZ – Eastern Carpathians Bend Zone; C – nappes of the Romanian Carpathian area. Age of deformation: J3 – Late Jurassic, K1 – Aptian–Albian, K2 – late Campanian–early Maastrichtian, Pg3?-M1 – (?)late Oligocene–early Burdigalian, M2 – middle Miocene (Răbăgia et al., 2011; Krézsek et al., 2013); D – modified regional cross-section from Schleder et al. (2019)

petrofacies (i.e. Cheia, Corbi formations) was also observed in the eastern Getic Depression (Roban, 2008; Fig. 1B). Răbăgia et al., (2011) considered that this facies migrated in time (early to late Oligocene) and space (from the Getic Depression towards the ECBZ and EC), being embedded within Pucioasa-like mudstones (i.e. Brăduleţ Formation in the Getic Depression) due to compression from the propagating foreland. Recently, Miocene foraminifera (e.g., *Trilobatus quadrilobatus, Globoquadrina dehiscens*) and calcareous nannoplankton (e.g., *Sphenolithus belemnos, Helicosphaera ampliaperta*) assemblages were identified by Szabo et al., (2010) and Szabo (2012) in the Pucioasa and Fusaru formations along the Pucioasa section (Fig. 2A, B).

The Vineţişu Formation (Grigoraş,1951 *fide* Popescu, 1952; Melinte and Brustur, 1998) consists of grey calcareous mudstones and some centimetre/metre-thick bentonitic tuffs (Vineţişu/Gura Vitioarei bentonites, Vălenii de Munte/Mlăcile tuffs), (Ştefănescu et al., 1993; Alexandrescu et al., 1994; Frunzescu, 2013; Fig. 3) with interbedded thin convolute fine-grained and bioturbated sandstones (Popescu, 1952; Szabo, 2012). Based on calcareous nannoplankton, this formation was considered uppermost Oligocene to lower Burdigalian (NP25–NN2) (Vineţişu, Lupa and Teleajen valleys – ECBZ; Mărunţeanu, 1999; Melinte and Brustur, 2008).

The following "upper dysodiles" and "menilites" (Olteanu, 1952; Bădescu, 2005) or Starchiojd Formation (Popescu, 2002 *fide* Frunzescu, 2013) consist of dark grey organic-rich shales (dysodiles) with some menilites and decimetre/metre-thick argillitized volcanic tuffs such as the Bătrâni Tuff (Popescu, 1952; Ştefănescu et al., 1993; Fig. 3). This formation is considered lower Burdigalian (Mărunţeanu, 1999), as it is placed between the Vineţişu Formation (NN2 Biozone) and Cornu Formation (NN3 Biozone).

The Slon Formation (Popescu, 1961 *fide* Bucur, 1966; Săndulescu et al., 1995) was considered Oligocene to lower Burdigalian (Ştefănescu, 1995) based on the type of facies which developed in the Vineţişu, Starchiojd and Cornu formations (Olteanu, 1952; Ştefănescu et al., 1988; Ştefănescu, 1995; Frunzescu, 2013; Fig. 3). This facies is characterized by chaotic deposits with reworked Cretaceous, Paleogene and lower Miocene age clasts embedded in a black/grey mudstone interpreted as olistostromes (Ştefănescu, 1995) and developed in the ECBZ (Olteanu, 1952) and EC (Joja, 1952). Ştefănescu (1995) described thick (100 m), massive, convolute sandstones with fine conglomerates in the upper part of the Fusaru Formation and suggested that these replace the Pucioasa-Fusaru facies towards the hinterland.

The deep marine setting was replaced by a shallow marine setting during the early Burdigalian (Schleder et al., 2019). This can be observed through the presence of the shallow marine Cornu Formation with the Sărata Gypsum that has an erosional contact with the top of the deep marine Pucioasa-Fusaru lithofacies (Mrazec and Popescu-Voiteşti, 1914; Mărunţeanu, 1999; Schleder et al., 2019; Filipescu et al., 2020; Fig. 3). These are followed by the unconformable Burdigalian–lower Badenian coarse-grained deltas of the Doftana Formation (*sensu* Ştefănescu and Mărunţeanu, 1980; Mărunţeanu, 1999). Recently, Filipescu et al. (2020) suggested that the Cornu and Doftana formations may be in reality younger (upper Badenian to Sarmatian).

METHODS

An ~6-km-long section with a series of exposures at Pucioasa (Fig. 2A) along the riverbed and riverbank of the Bizdidel Valley (N 45°5'45.80", E 25°26'51.99") was analysed by biostratigraphic, radiometric (zircon U-Pb dating on the Bătrâni Tuff), structural and sedimentological methods. The formations utilized in this study are based on the 1:50,000 Pucioasa map of Ştefănescu et al. (1988; Fig. 2A).

FIELDWORK AND SAMPLE COLLECTION

Detailed structural and sedimentological field observations and measurements of bedding, faults, fractures, folds and palaeocurrents were recorded. The structural measurements were taken using both a 360° Freiberg compass/clinometer and the *FieldMove*™ digital mapping application. The sense of fault movement was determined based on the presence of offset stratigraphic markers or kinematic indicators such as slickenlines or slikenfibres. Fault-slip slickenline data were collected *in situ* from exposed fault surfaces in order to perform a palaeostress inversion. In this study, the fault data were analysed using Angelier's (1990) direct inversion method (INVD) implemented in *SG2PS* software (Sasvari and Baharev, 2014). This method estimates the reduced stress tensor and the shear stress magnitudes from fault-slip data (Angelier, 1990). The program also graphically computes the stress regime based on the stress index (*R'*; Delvaux et al., 1997). Structural data processing and visualization were carried out using *Stereonet 10* (Allmendinger et al., 2012; Cardozo and Allmendinger, 2013). The measurements were graphically represented using both rose diagram plots of azimuth distributions (at 10° sector angles) and equal area stereonets, lower hemisphere projection using poles to planes where appropriate. The contouring was calculated after Kamb (1959) at 2 and 3 sigma standard deviation above a random population.

The cross-section was constructed in *Move* software suite following successive steps which includes: georeferencing and importing the 1:50,000 geological map of Ştefănescu et al. (1988), preexisting cross-sections (e.g., Stefanescu et al., 1988; Bercea et al., 2016; Schleder et al., 2019) and the Digital Elevation Model of the area. The structural measurements from the field (collected with coordinates) were also imported in the project and projected onto the cross-section. The next step involved the construction of the cross-section using all the data. In Move, we mainly used a tool called "horizon" from a template which allows the construction of the layers by keeping the thickness constant. The sedimentological data was obtained at centimetre/decimetre scale and included grain size (10x hand lens, Wentworth grain size comparator, ruler), lithology, bed contacts and sedimentary structures. The sedimentological data was grouped into facies and facies associations. Four synthetic logs were made starting from the two major anticline hinge lines having a thickness ranging from ~350 to 800 m. A 1 m Jacob staff with a 360° Freiberg compass was used for the thickness measurements. Quantitative palaeocurrent measurements were obtained and plotted in *SG2PS* (Sasvari and Baharev, 2014) software (modified in *CorelDraw2022*) although not re-tilted for tectonic dip correction (bedding dip <= 20°; Collinson et al., 2006). Also, 3 qualitative palaeocurrent (no dip correction) observations were made to ascertain the gross direction of flow for some asymmetrical ripples (Vineţişu Formation).

BIOSTRATIGRAPHY

The biostratigraphy was interpreted based on calcareous nannoplankton and foraminifera. Forty-one mudstone samples from the Pucioasa section (Fig. 2A) were analysed for calcareous nannoplankton content. The samples were prepared by the standard smear slides technique (Bown and Young, 1998) and examined under a light microscope (Axiolab A) in polarized

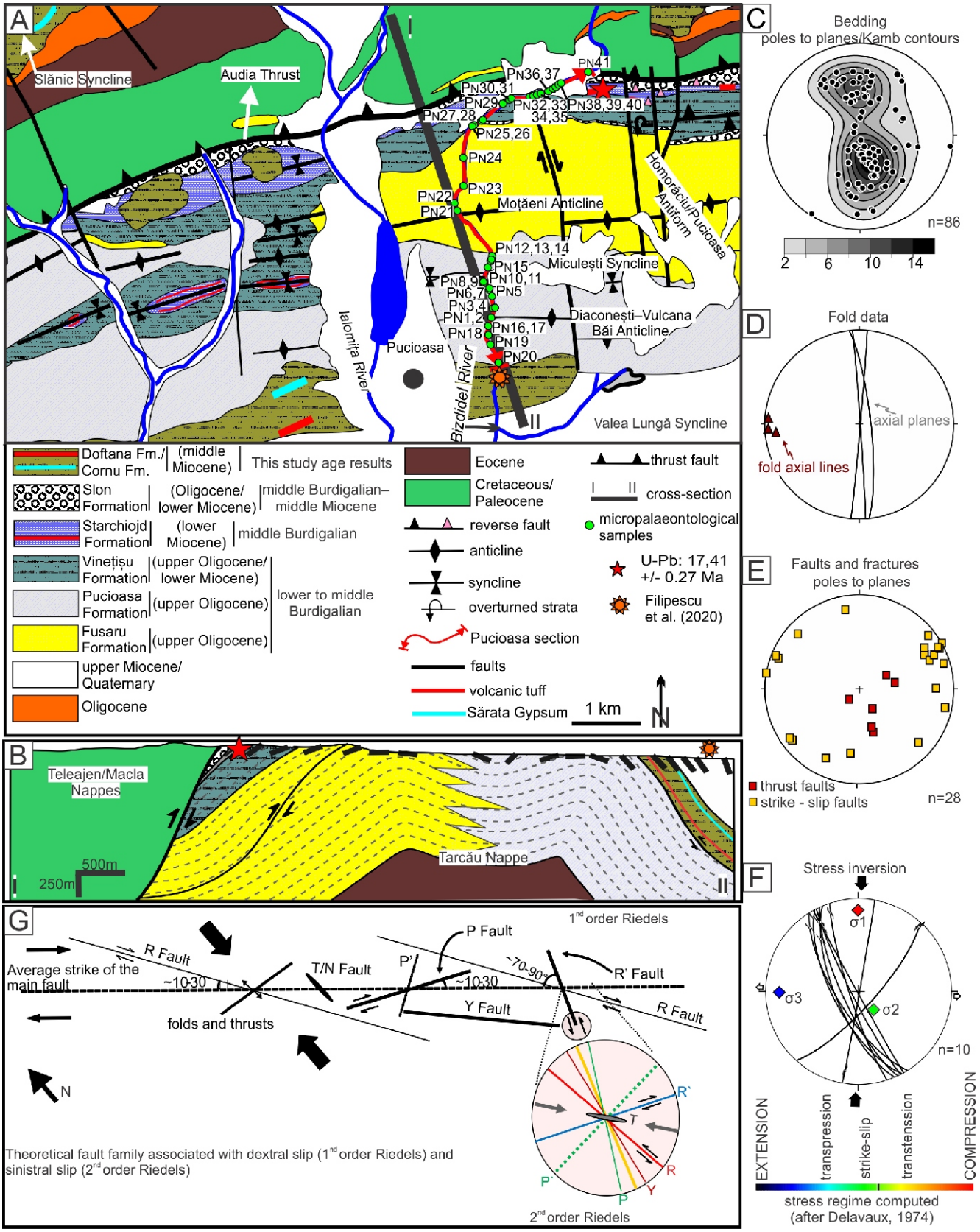

Fig. 2A – 1:50,000 modified geological map of the Pucioasa area (Ştefănescu et al., 1988); B – simplified cross-section using surface and subsurface published data (Ştefănescu et al., 1988; Schleder et al., 2019); C–E – stereonets of structural data collected in the field; F – stress inversion plot (after Angelier, 1990) of fault lineation data; G – theoretical fault family associated with dextral (1st order) and sinistral slip (2nd order; adapted after Carne and Little, 2012)

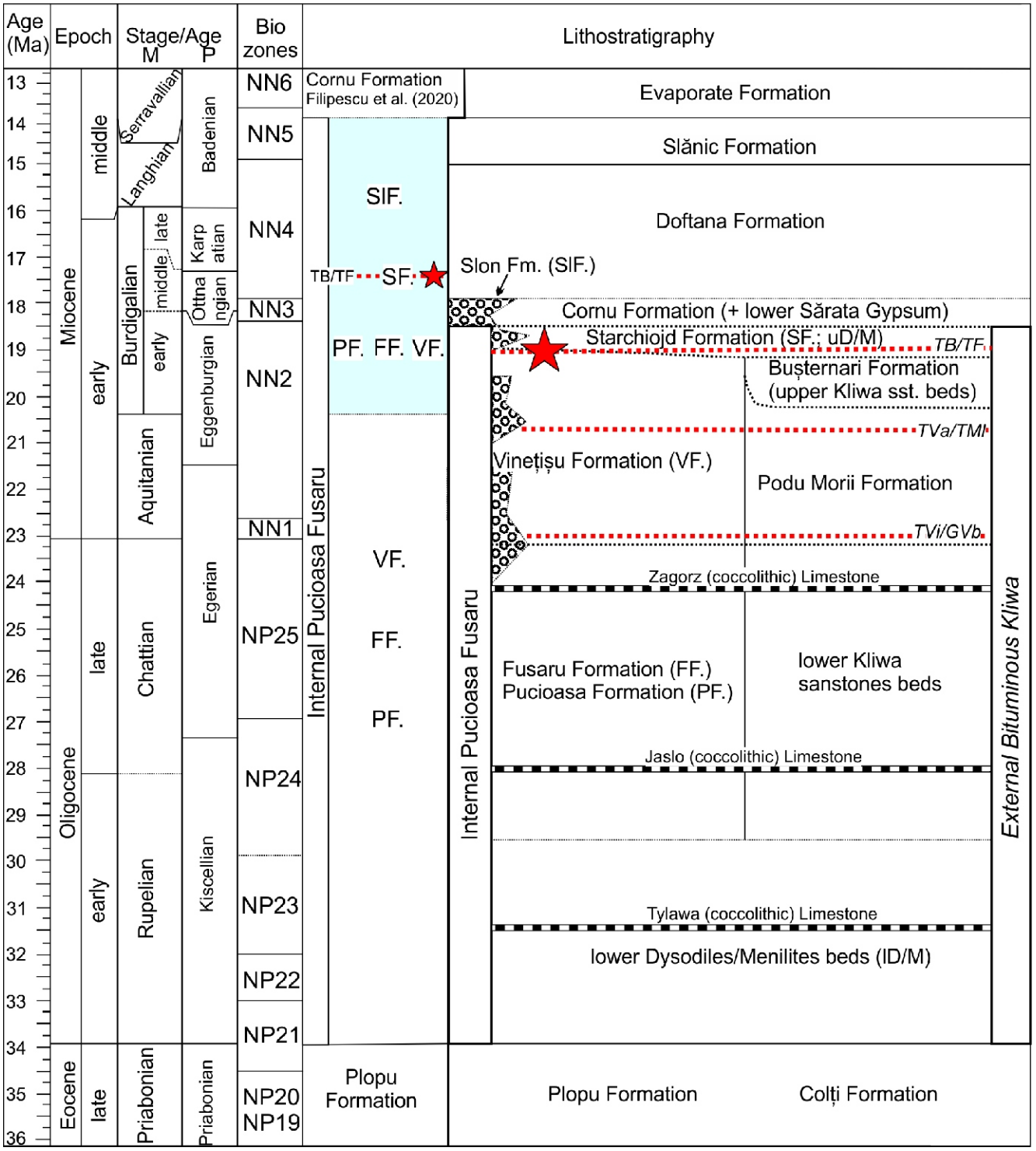

Fig. 3. Synthetic lithostratigraphic chart for the Tarcău (ECBZ) Nappe and this study (light blue color polygon)

Calcareous nannoplankton biozones based on Martini (1971) while the age distribution is from Raffi et al. (2020). Burdigalian division is based on Grunert et al. (2010). Lithostratigraphy uses information from Ştefănescu et al. (1988, 1993, 1995); Mărunţeanu (1999); Bădescu (2005); Melinte and Brustur (2008); Popescu (2002), *fide* Frunzescu (2013), Filipescu et al. (2020); UD/M – upper dysodiles and menilites. Discontinuous dotted red lines represent regional tuffs in the ECBZ/Eastern Carpathians: TVi (Vineţişu Tuff), GVb (Gura Vitioarei bentonites), TVa (Vălenii de Munte Tuff), TMl (Mlăcile Tuff), TB (Bătrâni Tuff), TF (Falcău Tuff; Ştefănescu et al., 1993; Alexandrescu et al., 1994; Frunzescu, 2013). Red star: UPb dated Bătrâni Tuff = 17.41 ±0.27 Ma. Depositional environment based on Conţescu et al. (1966), Ştefănescu (1995), Sylvester and Lowe (2004), Szabo (2012), Bercea et al. (2016), Schleder et al. (2019)

light, at 1000 x magnification. Biostratigraphic and palaeoecological information provided by foraminifera was interpreted using the material of Szabo (2012).

ZIRCON U-Pb DATING AND ZIRCON TRACE ELEMENT ANALYSIS OF THE BĂTRÂNI TUFF

U-Pb dating of the Bătrâni Tuff was done after separating zircons by heavy liquid density-based and magnetic methods from the 63–250 μm fractions. The zircon grains were mounted in 1“ epoxy resin and polished to a 1 μm finish. Before dating, the zircons were checked with optical microscopic and cathodoluminescence imaging. Cathodoluminescence imaging was produced using an *AMRAY 1830* SEM equipped with *GATAN MiniCL* and 3 nA, 10kV setup at the Department of Petrology and Geochemistry, Eötvös University in Budapest. The *in situ* zircon U-Pb isotopic and simultaneous trace element analyses were performed at the Department of Earth Sciences, ETH Zürich by laser ablation single-collector sector field inductively coupled plasma mass spectrometry (LA-SF-ICP-MS). Further instrumental, setup and data processing information are given in supplementary Appendices 1 and 2. Validation reference materials, covering an age interval between 1063.5 Ma and 2.409 Ma, were used to correct the matrix-dependent age offsets after Sliwinski et al. (2017). The average precision of the reference materials ranged from 1.2% to 2.3% (2se) in the case of secondary RM older than 30 Ma, while the youngest has 8.3% (2se) average precision. The Th disequilibrium correction was performed after alpha dose-correction assuming a constant Th/U partition coefficient ratio of 0.33 ±0.063 (1 ; Rubatto and Hermann, 2007) and using the equations of Schärer (1984). Zircon U-Pb dates were not corrected for common Pb contents; however, during data reduction, integration intervals were set to exclude the common Pb-contaminated signal intervals and data were filtered according to their discordance ([(^{207}Pb/^{235}U Age) – (^{206}Pb/^{238}U Age)] / (^{207}Pb/^{235}U Age) <10 %). Average uncertainty of the individual zircon dates is given as 2se and is 1.74% (rse). In the case of trace element analysis, we used NIST610 as primary reference material and zircon 91500 for quality control, and an in-house synthetic reference material (Synthetic Zircon Blank) to correct the Nb concentrations. Target elements were Si, Zr, REE, Y, Hf, P, Nb, Ta, U, Th, Ti (see Appendix 2), and Al, Ba were measured for monitoring glass and apatite inclusions. Si (15.2 wt.% in zircon) was used as an internal standard for data reduction done by IOLITE. Spot compositions contaminated with inclusions based on elevated Al, Ba and La contents were discarded from the interpretation.

RESULTS

The Pucioasa section is ~6 kilometres long and it extends between the Audia Thrust to the north and the northern margin of the Valea Lungă piggy-back syncline to the south (Fig. 2A). This section is along part of the Homorâciu anticline which is considered a major S/SSE-verging anticline, plunging to the west (Fig. 2A) and extending for at least 85 kilometres towards the east (e.g., Murgeanu et al., 1968). The Bizdidel River cuts the stratigraphy almost perpendicular to the structure of the Homorâciu/Pucioasa Antiform. The rocks exposed belong predominantly to the Fusaru, Pucioasa, and Vineţişu formations, with limited exposure of the Slon and Starchiojd formations to the north (Fig. 2A, B).

STRUCTURAL AND SEDIMENTOLOGICAL ASPECTS

STRUCTURAL STYLE

Close to the Audia Thrust, the beds dip generally moderately to steeply (~45 to 84°) to the N/NNW, and are highly deformed by closely spaced thrusts (a few metres apart) showing several repetitions of different formations. These thrusts most likely represent small-scale splays of the main Audia Thrust.

Away from the Audia Thrust, the beds typically dip gently to moderately (15–20°) to the N/NNW and S/SSE (Fig. 2B, D) and are deformed into large- (hundreds of metres) to small-scale (decimetre to metre) folds. Two large-scale anticlines (~1.6 kilometres wavelength), namely the Moţăeni and Diaconeşti-Vulcana Băi anticlines (Fig. 2A, B; Murgeanu et al., 1968), are separated by a syncline named here the Miculeşti Syncline (Fig. 2A, B). These folds are upright (axial plane 80–89°), gentle to open structures (interlimb angles of ~120–130°) and plunge shallowly (1–10°) towards the W (Fig. 2C). These folds are inferred to detach on top of the Eocene and be underlain by imbricate units of Eocene and Cretaceous rocks (Schleder et al., 2019; Fig. 1D). This structure is also called the Pucioasa Antiform (Fig. 2A; Schleder et al., 2019). Smaller-scale folds (some of chevron type) of similar orientation to the large-scale structures are encountered locally (Fig. 4A).

The sequence is cross-cut by numerous shallowly-dipping thrust planes to high-angle faults and fractures with multiple orientations and kinematics (e.g., Figs. 2F and 4B–F). The shallowly dipping (12-39°) thrust planes are NNW–SSE- and WSW–ENE-trending (Fig. 2F). The NNW–SSE-trending thrusts generally display kinematic indicators such as slickenline lineations showing reverse (slightly) oblique kinematics suggesting top-to the NNE movements (Fig. 4B). The WSW–ENE-trending thrusts generally display top-to-the-S movements (Fig. 2D). However, in the forelimb of the Diaconeşti-Vulcana Băi Anticline, a hinterland-verging thrust was encountered. The displacement on these thrusts is generally difficult to assess due to the lack of stratigraphic markers; however, some thrusts show displacements of only a few centimetres to ~1 metre (e.g., Fig. 4C).

The high-angle faults (57–98°) have two main trends (Fig. 2F): NNW–SSE and NNE–SSW. The NNW–SSE -trending faults dip steeply towards the WSW (Fig. 2F). Some of these faults, generally the smaller-scale ones, show tip-damage patterns such as horsetail splay structures, consistent with dextral slip (Fig. 4B; e.g., Kim and Sanderson, 2006). In addition, fault planes generally preserved slickenlines also suggesting dextral kinematics (Figs. 2F and 4F). These faults are sub-parallel with the previously mapped large-scale N–S- to NNW–SSE-trending dextral faults which offset the fold structures by up to ~300 m, to the east of the study area (Fig. 2A) (Ştefănescu et al., 1988).

The NNE–SSW-trending faults dip steeply towards the WNW (Fig. 2F). Some of these faults are associated with wide (~1 m) damage zones dominated by a network of closely spaced (centimetre to decimetre) fractures (Fig. 4D). These fracture populations are consistent with a sinistral strike-slip Riedel system (Fig. 2G). Moreover, some of these faults often preserved slickenlines on their fault planes consistent with sinistral slip (Fig. 4E). Locally, these high-angle strike-slip faults seem to crosscut the NNW–SSE- trending thrusts (Fig. 4G).

Those two sets, dextral and sinistral, developed at ~60° to each other, can represent first-order Riedel shear structures

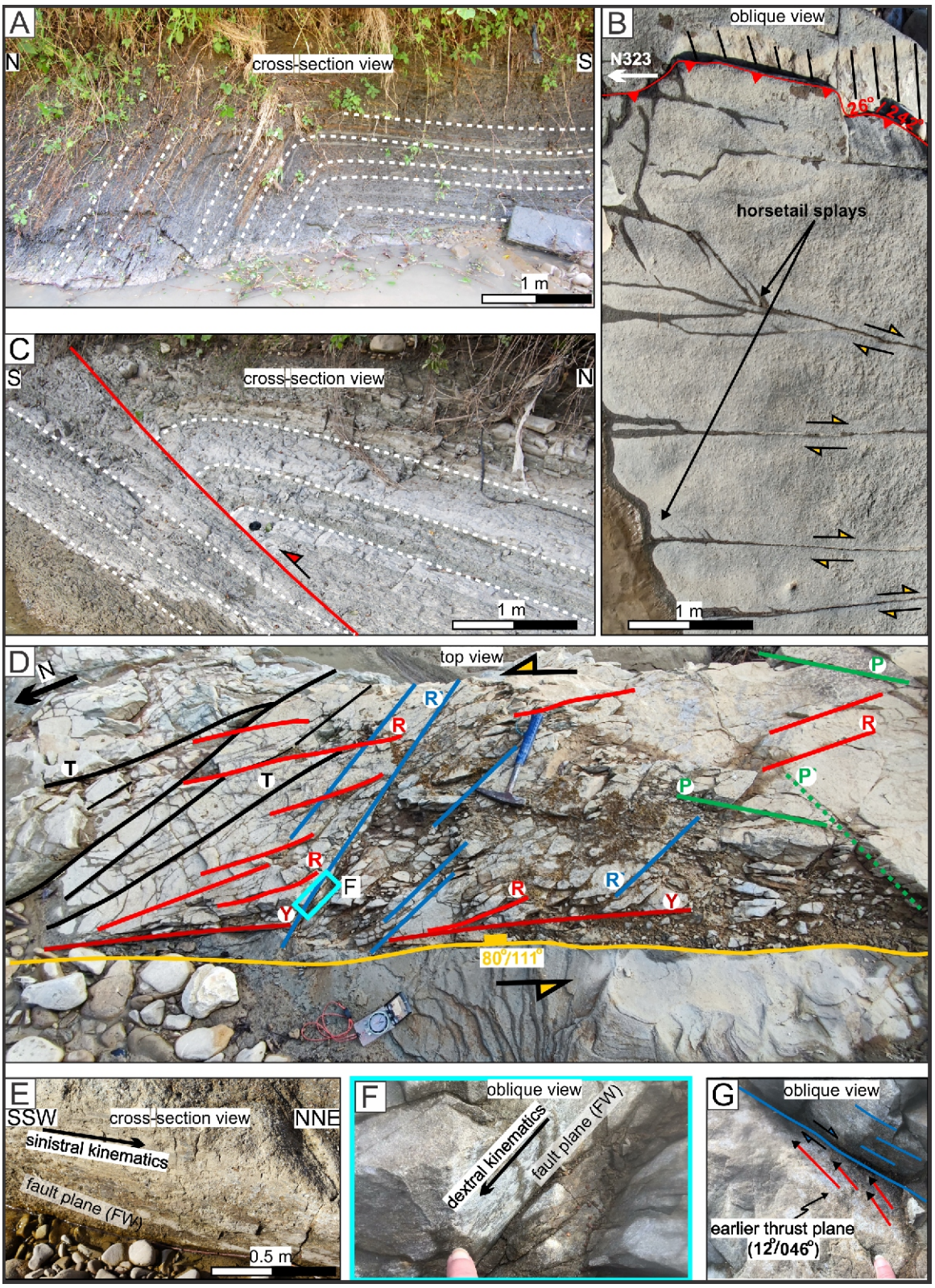

Fig. 4A – small-scale fold found close to the hinge line of the Diaconeşti-Vulcana Băi Anticline; B – horsetail splays with a thrust showing top-to-the-NNE movement (around Moţăeni Anticline); C – thrust with ~1 metre displacement (northern limb of Moţăeni Anticline); D – fractures related to a sinistral strike-slip Riedel system (Moţăeni Anticline); E – fault plane with slickenlines related to sinistral kinematics (Moţăeni Anticline); F – fault planes with dextral kinematics (Moţăeni Anticline); G – high-angle strike-slip faults that cross-cut the NNW–SSE-trending thrusts (Moţăeni Anticline)

developing simultaneously, as part of the same dextral strike-slip system (Fig. 2G). Palaeostress inversion analysis of these fault slip data yields a N-S compressive stress (Fig. 2F). The inversion suggests that the faults developed in a strike-slip to transtensional regime of near-horizontal compressive stress (1) with an axis orientated 16/002° and near-horizontal extensional stress (3) with an axis orientated 12/268° (Fig. 2F).

The N–S-directed compressive stress obtained is the same as the stress field suggested for the Wallachian phase (Hippolyte and Săndulescu, 1996). This stress field would also favor the development of the E–W-trending folds and the WSW–ENE-trending thrust (Fig. 2G). In addition, it is known that Wallachian folds present in the upper Miocene–lower Pleistocene strata are commonly large (interlimb angles of ~70–150°; Hippolyte and Săndulescu, 1996). Although developed in older stratigraphy, the folds observed in our study area are also gentle to open structures (interlimb angles of ~120–130°). It is very possible that these structures developed during the Wallachian phase together with the NNW–SSE-trending dextral faults (and associate Riedel shear structures) acting as tear faults which partitioned the E–W to WSW–ENE-trending contractional structures.

The NNW–SSE-trending thrusts identified in the study area (Fig. 4B, G) are more particular and do not seem to fit with the previously described (possibly) Wallachian structures. These thrusts, which are almost perpendicular to the E–W-trending folds and thrusts, are cross-cut by the high-angle strike-slip faults (Fig. 4G), suggesting their earlier development. It was previously suggested that the onset of deformation of the Tarcău Nappe, including the folds in the study area (Schleder et al., 2019), took place during the intra-Burdigalian phase (Săndulescu, 1984). It is possible that these structures are related to the pre-Wallachian events (intra-Burdigalian or Badenian-Sarmatian). A further regional study should be carried out to determine the nature and timing of these structures.

SEDIMENTOLOGY

The deposits analysed consist of several lithologies including mudstones, sandstones, slightly muddy sandstones, muddy sandstones, sandy to clast-supported conglomerates/breccias, muddy sandy conglomerates, muddy mud-clast conglomerates, volcanic tuffs, and organic-rich shales (dysodiles). They are associated with various sedimentary structures resulting in the description of 14 facies (F; Table 1). Those facies are grouped into 4 facies associations discussed below:

FACIES ASSOCIATION 1 (FA1): MUDSTONES WITH THIN- TO THICK-BEDDED SANDSTONES

The Pucioasa and Vineţişu formations (Figs. 2A, 3 and 5A1–A4) are characterized by F1 with thin-bedded very fine/fine sandstones (Fig. 6A–C) embedded in centimetre/metre thick dark/light grey (rare brownish/greenish) massive, laminated, graded mudstones (F2, Fig. 6D). Black organic-rich laminae are common in the mudstones. The sandstones are normally graded, have planar laminations, and asymmetrical and climbing ripples (Fig. 6A), with frequent muddy material on the foresets. The asymmetrical and climbing ripples can pass laterally/upwards into convolute lamination (Fig. 6C). Phytodetritus is frequent in the sandstones, the bases of which can be erosional to sharp. Rare centimetre-scale synsedimentary faults were observed. The medium-bedded muddy sandstones (F.3; Fig. 6E) and medium- to thick-bedded sandstones (F4; Fig. 6B, F) range from 10 to 80 cm-thick. The medium-bedded muddy very fine to fine sandstones (F3) are convolute with water escape structures and can have flat, erosional bases with mud rip-up clasts. F4 medium- to thick-bedded sandstones are normally graded, amalgamated with erosional to sharp bases and with asymmetrical ripples, convolutions and planar laminae. The latter can contain plenty of coalified phytodetritus (Fig. 6F). Thin structureless sandstone intrusions (F5) develop along fractures and appear as sill/dyke composites (Fig. 6G) and dykes (Fig. 6B).

Interpretation: the above-described deposits were deposited by low-density turbidity currents (F1+F2+F4; Tce, Tde, Tcde, Tbce; Bouma, 1965), high- to low-density turbidity currents (F4; Tabce) and slurry flows (F3; Lowe and Guy, 2000). F1 is characterized by grain-size breaks (bypassed sediments, Talling et al., 2012) and plenty of distal asymmetrical climbing ripples (high suspended fallout rates) deposited in non-uniform flows (Jobe et al., 2011). The closeness of FA1 to the confined coarse-grained depostis belonging to the Fusaru channel successions (discussed in detail below) (Fig. 5A1–A4) can explain the above structures through a gradient change when flow stripping occurred because of a lack of confinement. Also, the lateral/upwards change of traction sedimentation into convolute laminae shows a rapid and active sedimentation environment (Talling et al., 2012; Tinterri et al., 2016). The sandstone slurry deposits are transitional flows where turbulence was diminished by mud content (Lowe and Guy, 2000; Hubbard et al., 2009). Lofting deposits (Zavala and Arcuri, 2016; Fig. 6F) may reflect extrabasinal hyperpycnal flow together with the graded mudstones and coalified phytodetritus. We interpret FA1 as a deep marine levee/overbank (F1, F2) setting with overbank elements such as crevasse splay lobes (F3, F4; Fig. 7; Hubbard et al., 2009). We interpret the structureless sandstone intrusions as post-depositional injectites over pressured fluidized sandstones (Duranti and Hurst, 2004) that may relate to a contractional regime as found elsewhere in the ECBZ (see Tămaş et al., 2020).

FACIES ASSOCIATION 2 (FA2): CONFINED SANDSTONES AND CONGLOMERATES

This represents the Fusaru Formation (Figs. 2A, 3 and 5A1, A2) and consists of very fine to very coarse medium-bedded/graded sandstones, medium/thick-bedded slightly muddy sandstones and structureless sandstones (decimetre- to metre-thick) (F6, F7, F8). F6 has normal to reverse graded sandstones, traction sedimentation structures such as cross-stratification, planar (Fig. 6H), asymmetrical and climbing ripple lamination (Fig. 6I). Normally graded slightly muddy very fine to fine sandstones with frequent asymmetrical ripples, planar and some convolute laminae develop within F7. Normally graded, amalgamated, structureless sandstones characterize F8 (Fig. 6I–K). The sandstone bases can be flat to erosional or with load casts (isolated load balls; F8; Fig. 6I) and flames. Mudstone rip-up clasts are frequent, and rarely can reach 80 cm on the long axis (F8; Fig. 6J). Thin F2 beds can be interbedded between F8-type sandstones (Fig. 6K). Centimetre-thick lenses of coarse/very coarse sand and scattered granules (locally imbricated – (a[p]a[i])) develop in some sandstones (F8, F6). The conglomerates can be sandy to clast-supported (F9; Fig. 6L) or can appear as disorganized muddy sandy conglomerates (F10; Fig. 6M). The conglomerates can be structureless (F10) and/or reverse to normally graded (F9; Fig. 6N) with flat to erosional bases (mudstone rip-up clasts). They have a grain size ranging from fine pebbles to large cobbles and rare boulders (limestones). A few breccias were observed in F9. Deformed mudstone- sandstone couplets charac-

Table 1

Description and interpretation of the facies from Pucioasa section

Facies		Primary sedimentary structures/Bed thickness	Other features	Processes, depositional environment	Figure
Thin bedded sandstones	**F1**	1–10 cm grey vf/f sandstones (frequent 1–5 cm) between 2–50 cm thick mudstones. Ripples and climbing ripples, convolute lamination, load casts, rare faint planar lamination, often normal grading. Flutes to sharp bases. Muddy foresets. Rippled sandstones can evolve laterally, upward in convoluted sandstone.	Siltstones and vf sandstone laminae (ripples). Frequent phytodetritus. Rare small scale synsedimentary faults. Micas, sulphur, oxides in sandstones.	Low density turbidity flows (Tce, Tde, Tcde, Tbce) (Bouma, 1962, Talling et al., 2012). Traction sedimentation, excess pore pressure/rapid sedimentation (Mulder and Alexander, 2001; Talling et al., 2012). Distal levee/overbank setting of a channel (Hubbard et al., 2009; Fongngern et al., 2018).	**6A–C**
Massive, laminated, graded mudstones	**F2**	Structureless, planar parallel lamination to discontinuous/faint lamination (mm coarse silt laminas) in mudstones. Cm to m in thickness.	Dark/light grey, rare brownish/greenish coloured calcareous mudstones. Black organic rich laminae. Locally, organic matter is high but not like in F12. Silt content in mudstones can vary (normal/reverse graded). Phytodetritus (can be coalified). Pyrite, micas.	Hemipelagites, pelagites, diluted low density turbidity flows (Te, Tde) (Bouma, 1962; Talling et al., 2012). Some depostis could be related to muddy hyperpycnal flows of extrabasinal turbidites (Zavala and Arcuri 2016).	**6D**
Medium bedded muddy sandstones	**F3**	20–60 cm very fine/fine muddy sandstones. Frequent convoluted laminations, water escape structures. Flat to erosional sandstone base.	Phytodetritus, micas.	Slurry deposits (Lowe and Guy, 2000). Fan fringes, overbank crevasse splay lobes (Hubbard et al., 2009).	**6E**
Medium to thick bedded sandstones	**F4**	10–80 cm f sandstones, normal graded and amalgamated. Erosional/sharp base. Rippled, convoluted and planar laminated sandstones. Rare <3 cm thick bended muddy sandstones with ripples/convoluted lamination intercalations exists. Rare planar lamination made from coalified phytodetritus.	Cm thick lenses of c/vc sand grains. Phytodetritus, micas.	High density to low density turbidity flows (Tabce, Tbc, Tc; Bouma, 1962). Hindered settling, traction sedimentation (Mulder and Alexander 2001; Talling et al., 2012). Convoluted beds probably due to rapid sedimentation/excess pore pressure (Owen & Moretti 2011; Talling et al., 2012). Probably lofting deposits/hyperpycnal flows (Zavala and Arcuri, 2016). Fan fringes, overbank crevasse splay lobes (Hubbard et al., 2009).	**6B, F**

Tabl. 1 cont.

Facies		Primary sedimentary structures/Bed thickness	Other features	Processes, depositional environment	Figure
Centimetre to metre thick fluidized sandstones, fine conglomerates	**F5**	Structureless. Cm to m thick deposits.	Discordant with the host rock (dykes). Sills (undulating tops) and composite sill-dyke. Abrupt lateral terminations, chaotic intrusion swarms (host rock inclusions). Some injectites develop along fractures. Sandy fine conglomerates were observed.	Formed by overpressured and fluidized sandstones, sandy fine conglomerates intruded in background rocks (Duranti and Hurst, 2004) as injectites.	**6B, G**
Medium bedded graded sandstones	**F6**	30–60 cm normal graded, reverse to normal graded vf/f sandstones. Can stack >3 m in thickness. Planar lamination, cross stratification, asymmetrical climbing ripples and ripples. The last two can evolve laterally in convolute laminations.	Rare vf granulley sandstones (± pebbles) at the base of sandstones. Cm thick lenses of c/vc sand grains/scattered granulles in sandstones. Sheared flames, load casts. Amalgamated sandstones, dish structures. Phytodetritus, micas.	Traction, traction carpets, rapid fall out sedimentation (S1, S2, S3/Ta) related to high density turbidity currents (Lowe, 1982; Talling et al., 2012) to low density turbidity currents (Tbc; Bouma, 1962). Channel fills in Fusaru/Slon formations. In Slon Formation, formed by filling/overflow of the negative/positive topography of the MTC	**6H, I**
Medium to thick bedded slightly muddy sandstones	**F7**	20–120 cm vf/f sandstones (frequent 20–50 cm) with some amount of muddy matrix. Normal graded, frequent asymmetrical ripples and planar lamination.	Amalgamated. Bioclasts. Rare convolute lamination. Phytodetritus, micas.	High/low density turbidity deposits (Ta, Tabc, Bouma, 1962; Talling et al., 2012), (?)slurry deposits (Lowe and Guy, 2000). Confined (Sprague et al., 2005) channel fills elements in Fusaru Formation.	
Medium to thick bedded structureless sandstones.	**F8**	40–100 cm that stack up to maximum 15 m in thickness, f to vc sandstones. Normal graded to no grading. Structureless. Often amalgamated. Dish structures. Flat to erosional base. Load casts (+isolated load balls).	Mudstones rip up clasts (<80 cm in size). Cm thick lenses of c/vc sand grains/ scattered granulles. Alternating with F2 (rare). Rare cm/dm thick rippled, convoluted stack f sandstones toward the top. Muddy foresets. Phytodetritus. Sheared flames, micas.	S3 type sandstones (Lowe, 1982) formed by rapid sedimentation related to a high density turbidity flow followed (rare) by low density turbidity currents (Tc; Bouma, 1962). Confined (Sprague et al., 2005) fills in Fusaru Formation.	**6I, J, K**
Clast supported - sandy conglomerates/ breccia	**F9**	Structureless, reverse to normal graded. Dm thick that can stack >3 m in thickness. Flat, erosional base. Granulles to very rare boulders (some limestones).	Micas, bioclasts.	Traction carpet and traction sedimentation related to high ,density turbidity currents (R2, R3; Lowe, 1982). Confined channel fills (Sprague et al. 2005) in Fusaru Formation.	**6L, N**

Tabl. 1 cont.

Facies		Primary sedimentary structures/Bed thickness	Other features	Processes, depositional environment	Figure
Disorganized muddy sandy conglomerates	**F10**	Structureless, rare grading. Dm/m thick beds. Grain size of conglomerates: up to 25 cm.	Mud clasts of various grain size (granulles to pebble). Micas.	*En masse* cohesive freezing of debris flows (Dm2 of Talling et al., 2012). Confined channel fills (Sprague et al., 2005) in Fusaru Formation.	**6M**
Slumped mudstones-sandstones couplets	**F11**	None in place. Metre in thickness	Faulting with some synkinematic sedimentation. F7 type sandstones. Onlap strata terminations. Rich in phytodetritus.	Levee slump failure. Related to the confined channel fills (Sprague et al., 2005) in Fusaru Formation.	**6O**
Organic rich shales (dysodiles)	**F12**	Structureless. Centimetre to metre in thickness.	Fissility. Coalified plant material (often), sulphur, gypsum efflorescence. F2, F13 intercalations appear around the base.	Hemipelagites, pelagites. Anoxic conditions due to palaeogeographic isolation (Amadori et al., 2012) with short term anoxic disruptions (F2 presence).	**6P**
Volcanic tuffs	**F13**	Massive, normal graded. Parallel laminated, asymmetrical ripples develop with dark muddy material on foresets. Convolute laminations. Cm/dm in thickness that stack up to <3 m in thickness.	Rare coal clasts, phytodetritus. Interbedded with F12.	Volcanic ash fall out reworked as diluted low density turbidity flows. Traction sedimentation. Ștefănescu et al., (1993) considered this type of tuffs in the ECBZ as deposited by bottom currents.	**6Q**
Chaotic m thick muddy sandstones and mud-clast conglomerates	**F14**	Structureless, chaotic bedding. Can stack >200 m in thickness. The thickness can be affected by reverse faults and covered intervals. One 2 m thick chaotic muddy vf sandstone bed.	Frequent cm thick organic rich shalestones (F12) clasts and cm to m thick greenish-reddish Cretaceous-Paleogene mudstones clasts. Interlayered around the base with m thick F12. Coal clasts, micas.	Caused by active compression tectonics that triggered mass failure of the upper slope/shelf edge that formed cohesive muddy debris avalanches/mass transport complexes (Moscardelli and Wood, 2008; Hubbard et al., 2009; Dm2 of Talling et al., 2012). *En masse* cohesive freezing (Lowe 1982; Mulder and Alexander, 2001). Deposited on the base of slope/basin floor (foredeep or wedge top basins). The F12 intercalation, can be an olistolite or structural repetition.	**6R**

terize F11 (Fig. 6O) that contain mostly F7-type sandstones. Onlap wedge strata terminations were identified in F11 at ~330 m (Figs. 5A1 and 6O). Structureless sandstones and sandy granules were seen injected (F5) into background mudrocks as dykes, forming intrusion swarms and abrupt lateral terminations. An interesting feature is some horizontal/sub-horizontal beds of F6, F7 with onlap terminations on erosional surfaces, at around 0–50 m (Figs. 5A1 and 8). These appear as organized lateral stacking (Funk et al., 2012) architectures (Fig. 8), migrating from south to north, locally with thin F2-type margin drapes (McHargue et al., 2011). Here palaeoflow measurements from sandstone flutes show transport to the ESE (Fig. 5A1, B). The last two observations indicate a gross west to east flow. The lateral stacking packages have an overall coarsening-upwards trend (Fig. 5A1).

Interpretation: The facies described in FA2 was deposited by high- to low-density turbidity currents (F2, F6–F9; Fig. 6H–L, N), cohesive debris flows (Dm2 of Talling et al., 2012; F10; Fig. 6M), slumping (F11, Fig. 6O) and fluidized overpressured sandstones – injectites (F5). In the low-density turbidity deposits, traction sedimentation relates to Tb, Tc and in places with Td/Te (Bouma, 1962; F6–F8, F2). The high-density turbidity deposits are interpreted as R2/R3 sequences of Lowe (1982) (F9; Fig. 6L, N) for conglomerates, deposited as traction carpets with rapid fallout sedimentation. For sandstones, S1–S3/Ta sequences (Bouma, 1962; Lowe 1982), (F6–F8; Fig. 6H–K) were interpreted as deposited by traction, traction carpets and suspension sedimentation. Cohesive debris flows (F10; Fig. 6M) were deposited through *en-masse* cohesive freezing (Talling et al., 2012). F11 (Fig. 6O) with deformed strata and synkinematic sedimentation (onlap/wedge) related to a slump failure on a levee made from F7/F2. We interpret FA2 of the Fusaru Formation as confined channel deposits (Sprague et al., 2005; Figs. 5A1, A2 and 7). The horizontal/sub-horizontal (Fig. 8B) beds between erosional surfaces (Fig. 8C–E) are typical of cut-and-fill geometries related to channel avulsion (Abreu et al., 2003).

FACIES ASSOCIATION 3 (FA3): ORGANIC-RICH SHALES WITH MUDSTONES AND VOLCANIC TUFFS

FA3 describes the Starchiojd Formation with the Bătrâni Tuff (Figs. 2A, 3 and 5A1). F12 is composed of organic-rich fissile shales (dysodiles; Fig. 6P) with coalified phytodetritus, sulphur, gypsum efflorescences and some F2 mudstone interbeds. Also, two decimetre-/metre-thick grey-whitish, sometimes with reddish-brown coloured crusts, volcanic argillized plastic tuff packages (F13; Fig. 6Q) are developed, separated by 4-m-thick dysodiles. The tuff can be normal graded, massive or with planar, asymmetrical ripple and convolute laminae, interbedded with thin F12 rocks. Dark muddy material develops on the foresets of the asymmetrical ripple laminae (Fig. 6Q). The palaeocurrent flow (no dip correction) of the asymmetrical ripple laminae shows a trend to the SW.

Interpretation: The dysodiles were formed due to anoxic conditions related to basin palaeogeographic isolation (Amadori et al., 2012). These deposits were considered by Ştefănescu et al. (1993) to be a regional marker that drapes the older rocks (Fig. 7E). Brief anoxic disruptions are signaled by the presence of F2-type rocks (Fig. 5A1). The volcanic tuffs were deposited by low-density turbidity currents, given the numerous asymmetrical ripple laminae. Ştefănescu et al. (1993) interpreted some lower Miocene tuffs with asymmetrical ripple laminae from the ECBZ as deposited by marine bottom currents.

FACIES ASSOCIATION 4 (FA4): CHAOTIC MUDDY CONGLOMERATES WITH ORGANIZED SANDSTONES

This characterizes the Slon Formation (Figs. 2A, 3 and 5A1) and consists mostly of structureless/disorganized muddy conglomerates (F14; Fig. 5A1). Centimetre-thick dysodile clasts and centimetre- to metre-thick greenish-reddish (Fig. 6R) mud clasts, originating from the nappes immediately to the north, were observed in a grey mudstone matrix. Around the base (~625 m – Fig. 5A1) interbedded non-chaotic metre-thick organic-rich dysodiles (F12) are present. F6-type metre-thick amalgamated normally graded sandstones with mud rip-up clasts, pebbles, asymmetrical ripple laminae and phytodetritus were identified near the top.

Interpretation: The F4 deposits were interpreted as mass transport complexes (MTC; Moscardelli and Wood, 2008) related to active compression tectonics (hinterland nappe stacking) that triggered mass failure of the upper slope/shelf edge (Fongngern et al., 2018; Fig. 7D, E). This formed cohesive muddy debris avalanches (Hubbard et al., 2009; Dm2 of Talling et al., 2012) that settled through *en masse* cohesive freezing (Lowe,1982, Mulder and Alexander, 2001). They were deposited around the base of the slope/basin floor (foredeep or wedge-top basins). The organized sandstones (F6) were deposited by high/low turbidity currents (Tac; Bouma, 1962) probably by filling the negative topography of (ponding in) the mass transport complexes. The metre-thick F12 may be a slide block (olistolith) from FA3, the result of *in situ* sedimentation disrupted by mass transport complexes, or a structural repetition. Due to poor exposure, interpretation is difficult.

BIOSTRATIGRAPHY

CALCAREOUS NANNOPLANKTON

The calcareous nannoplankton assemblages (Table 2) are characterized by a low to low/medium diversity, fluctuating abundance, and poor to moderate preservation. Due to the structural settings and sedimentation that can involve significant solids reworking, the identification of certain biozones was locally difficult. From the Diaconeşti–Vulcana Băi Anticline with Pucioasa Formation deposits (Ştefănescu et al., 1988) 16 samples were collected (PN1–PN11, PN16–PN20) and two logs were constructed (Fig. 5A3, A4).

The northern limb samples (PN1–PN11; Fig. 5A3) of this anticline are of moderate abundance and preservation and low/moderate diversity. Here, *Helicosphaera ampliaperta* (Fig. 9A) was identified in four samples (Table 2). As this species has its first occurrence within the NN2 Biozone (base Burdigalian; Mărunţeanu, 1999; Raffi et al., 2020) we interpret log 3 (Fig. 5A3) from the Pucioasa Formation as not older than Burdigalian (NN2 Biozone).

The southern limb of the Diaconeşti–Vulcana Băi Anticline (PN16-PN20; Fig. 5A4) is characterized by low abundance and diversity (Table 2) and poor preservation of the calcareous nannoplankton compared to the northern limb (Fig. 5A3). The first occurrence of *Helicosphaera scissura* (Fig. 9B) and *Reticulofenestra pseudoumbilicus* (<7 μm) (Fig. 9C) in the Paratethys were recorded in the NN1 Biozone and respectively at the base of the NN2 Biozone of the Aquitanian (Mărunţeanu, 1999; Melinte and Brustur, 2008; Kováč et al., 2017; Raffi et al., 2020). Young et al., (2017) proposed the first occurrence of *R. pseudoumbilicus* in the NN4 Biozone and the first occurrence of *Helicosphaera scissura* in the upper part of the NN2 Biozone. Therefore, we interpret log A4 (Fig. 5A4) of the Pucioasa For-

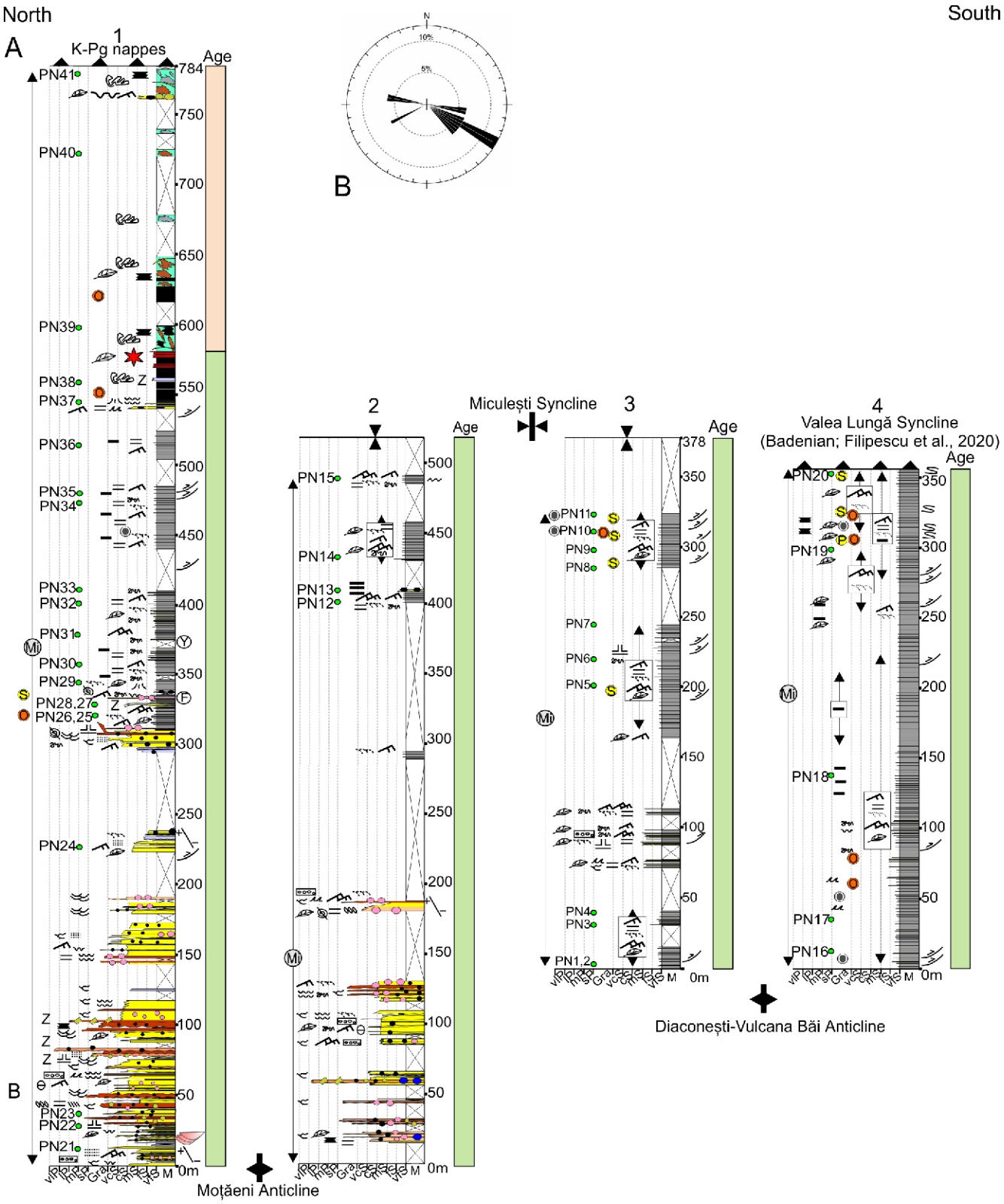

Fig. 5A – synthetic logs (1, 2, 3, 4) of the Bizdidel Valley showing the U/Pb and calcareous nannoplankton samples (see text for more details); B – some palaeocurrent measurements from Fusaru Formation sandstones (flutes and groove marks) – location log 1 base

vlP – very large pebbles, lP – large pebbles, mP – medium pebbles, sP – small pebbles, Gra – granulles, vcS – very coarse sands, cS – coarse sand, mS – medium sand, fS – fine sand, vfS – very fine sand, M – mudstone

mation as not older than Aquitanian (NN2 Biozone). Log 2 (Fig. 5A2) is situated in the southern limb of the Moţăeni Anticline (PN12–PN15) and was sampled only from mudstones of the Pucioasa Formation (Ştefănescu et al., 1988). It shows low/medium abundance, preservation and diversity (Table 2). *Helicosphaera ampliaperta* appears in all the samples investigated, and *Sphenolithus heteromorphus* (Fig. 9D,E) and *Helicosphaera walbersdorfensis* only in one sample (PN14). The first occurrence for the last two species noted is placed around the base of the NN4 Biozone (Young et al., 2017; Boesiger et al., 2017), although in the Paratethys realm *Helicosphaera walbersdorfensis* has been recorded from the upper part of the NN4 Biozone (Hohenegger et al., 2009) or higher , perhaps even in the NN6 Biozone (Mărunţeanu, 1999). Based on the co-occurrence of *Helicosphaera ampliaperta*, *Sphenolithus heteromorphus* and *Helicosphaera walbersdorfensis* and the closeness of the samples, we interpret log 2 (Fig. 5A2) of Pucioasa Formation as not older than Burdigalian (NN4 Biozone).

In the northern limb of the Moţăeni Anticline, 8 samples (PN21–PN28; Fig. 5A1) were taken from the mudstones found in the Fusaru Formation. These are of It has a low/moderate diversity and high abundance. *Sphenolithus belemnos* was identified in one sample (PN28) while *Helicosphaera ampliaperta* was observed in 4 samples (Table 2). *Sphenolithus belemnos* was identified within NN3 Biozone (Mărunţeanu, 1999) or in the upper part of the NN2 Biozone (Raffi, 2020). For this exposure an age not older than Burdigalian (NN2–NN3 Biozones) was interpreted.

The mudstones of the Vineţişu Formation (Fig. 5A1) showed a high abundance and low/medium diversity of species. Here, a more consistent appearance of *Helicosphaera ampliaperta* was observed (7 samples) together with a few specimens of *Helicosphaera walbersdorfensis* (PN30, PN34; Fig. 9F). Thus, based on the co-occurrence of these species we interpret this section as not older than Burdigalian (NN4 Biozone). One sample (PN 38) was taken from the Starchiojd Formation but it proved to be barren. Three samples were taken from Slon Formation (PN39–PN41) and they contained a few Miocene species (*Reticulofenestra haqii, Reticulofenestra pseudoumbilicus*) together with some long-ranging taxa (*Coccolithus pelagicus, Sphenolithus moriformis, Discoaster deflandrei, Reticulofenestra bisecta*).

THE BIOSTRATIGRAPHIC RE-EVALUATION OF PUBLISHED CALCAREOUS NANNOPLANKTON

Even though the formations were interpreted as Oligocene and Oligo-Miocene on the 1:50,000 geological map of Ştefănescu et al. (1988; Fig. 2A and Table 3), the associated calcareous nannoplankton may be interpreted differently. The presence of *Helicosphaera ampliaperta* in the Fusaru and Pucioasa formations indicates a Burdigalian age (not older than NN2 Biozone). The occurrence of *Helicosphaera ampliaperta* and *Sphenolithus belemnos* in the Vineţişu Formation indicates a Burdigalian age (NN2–NN3 Biozones) while *Sphenolithus heteromorphus* was identified only in the Starchiojd Formation which indicates a Burdigalian age (NN4 Biozone).

FORAMINIFERAL BIOSTRATIGRAPHY

The small number of planktonic foraminifera in most of the samples investigated and their mixed ages suggest that the specimens may have been sorted during transport and reworking. Rare local abundances (close to PN31 to PN34 in the Vineţişu Formation and around PN24 in the Pucioasa Formation) may be associated with marine flooding events. Two types of planktonic foraminiferal assemblages were distinguished: i) those with small globigerinids (*Tenuitella*, *Globigerina* – e.g. around PN20) reflecting eutrophic conditions (Filipescu and Silye, 2008; Beldean et al., 2012) and ii) those with large globigerinids (*Trilobatus*, *Globoquadrina* – e.g. south of sample PN32) typical of oligotrophic conditions of transgressive intervals.

The presence of *Trilobatus quadrilobatus* (e.g. around sample PN29; first occurrence in the Aquitanian M1a Zone of Wade et al., 2011; Fig. 9G), *Trilobatus subsacculifer* (e.g. around sample PN29; first occurrence in the Aquitanian M1b Zone; Fig. 9H), *Globoquadrina dehiscens* (e.g. around sample PN29, PN31–PN32; first occurrence in the M1b Zone), and *Tenuitella*

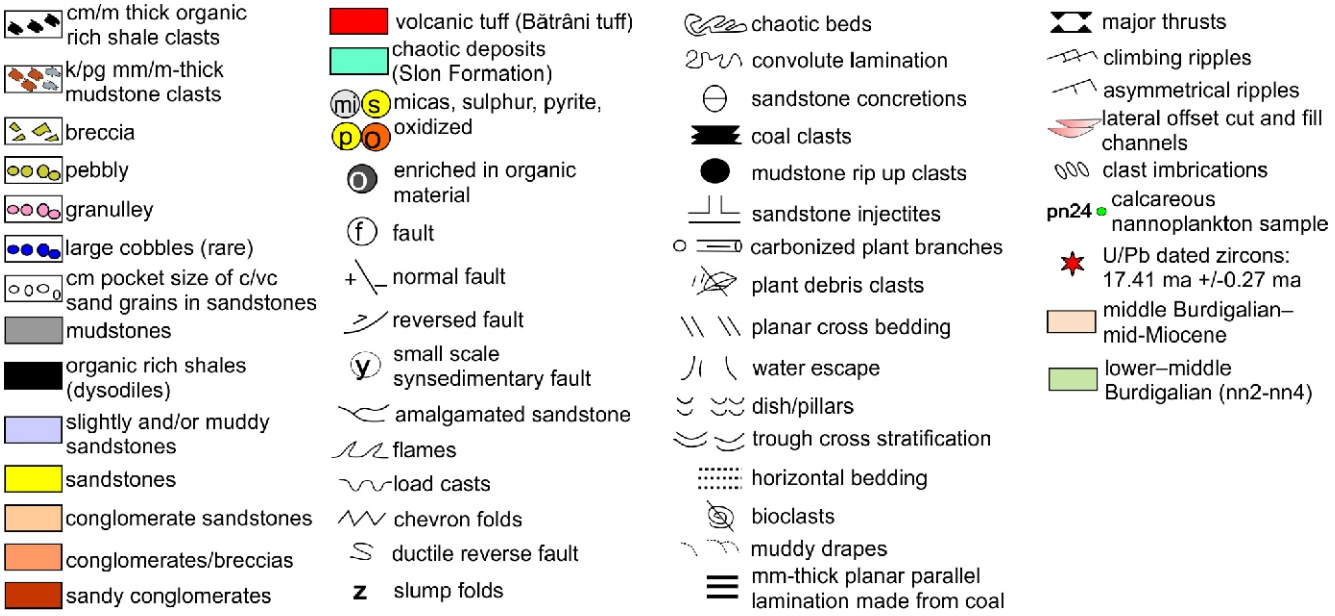

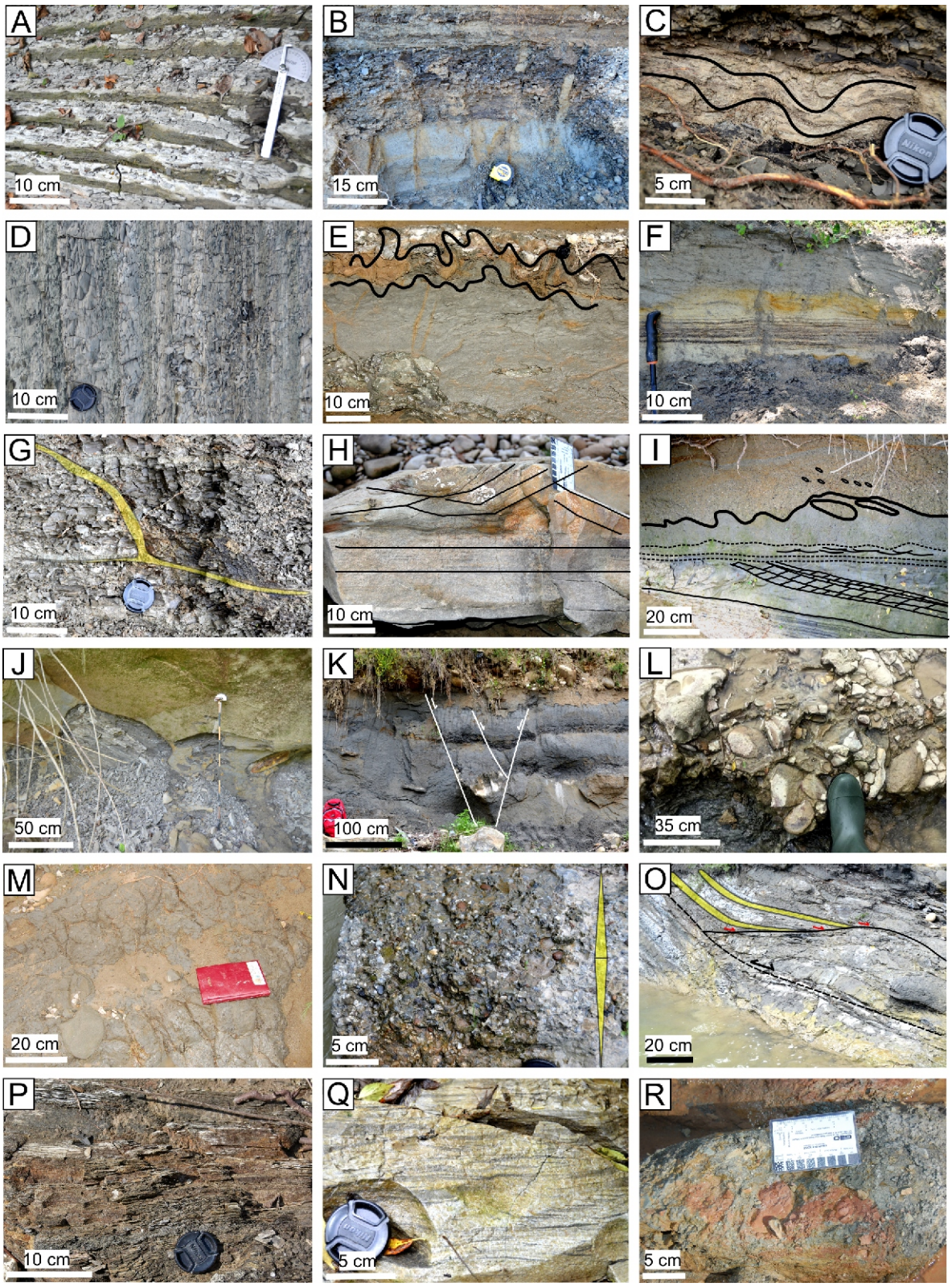

Fig. 6A – thin-bedded vf/f sandstones with asymmetrical ripples (F1); B – thin/medium-bedded vf/f sandstones with sandstone injectite dykes (F1, F4, F5); C – thin-bedded convolute vf sandstone (F1); D – massive/laminated graded mudstones (F2); E – erosional medium-bedded muddy sandstone with convolute and water escape structures (F3); F – thick-bedded normally graded fine sandstone with coalified planar laminae (F4); G – sill/dyke composite vf sandstone injectites (F5); H – medium-bedded f/m planar laminated to cross-stratified sandstone (F6); I – medium-bedded and graded f/m sandstones (F6) eroded by thick-bedded structureless f/m sandstones with imbricated clasts (+ isolated load balls), (F8); J – thick-bedded structureless m/c sandstones with decimetre-thick rip-up mud clasts (F8); K – normal faulted medium-thick bedded structureless f/m sandstones (F8) with rare thin F2 interbedding; L – clast-supported conglomerates/breccia (F9); M – disorganized muddy sandy conglomerates (F10); N – normal to reverse graded sandy vf conglomerates (F9); O – slumped beds with synkinematic sedimentation (red arrows – onlaps), (F11); P – organic-rich shales (dysodiles), (F12); Q – volcanic tuff with tractional structures (F13); R – chaotic muddy mud-clast conglomerates (F14)

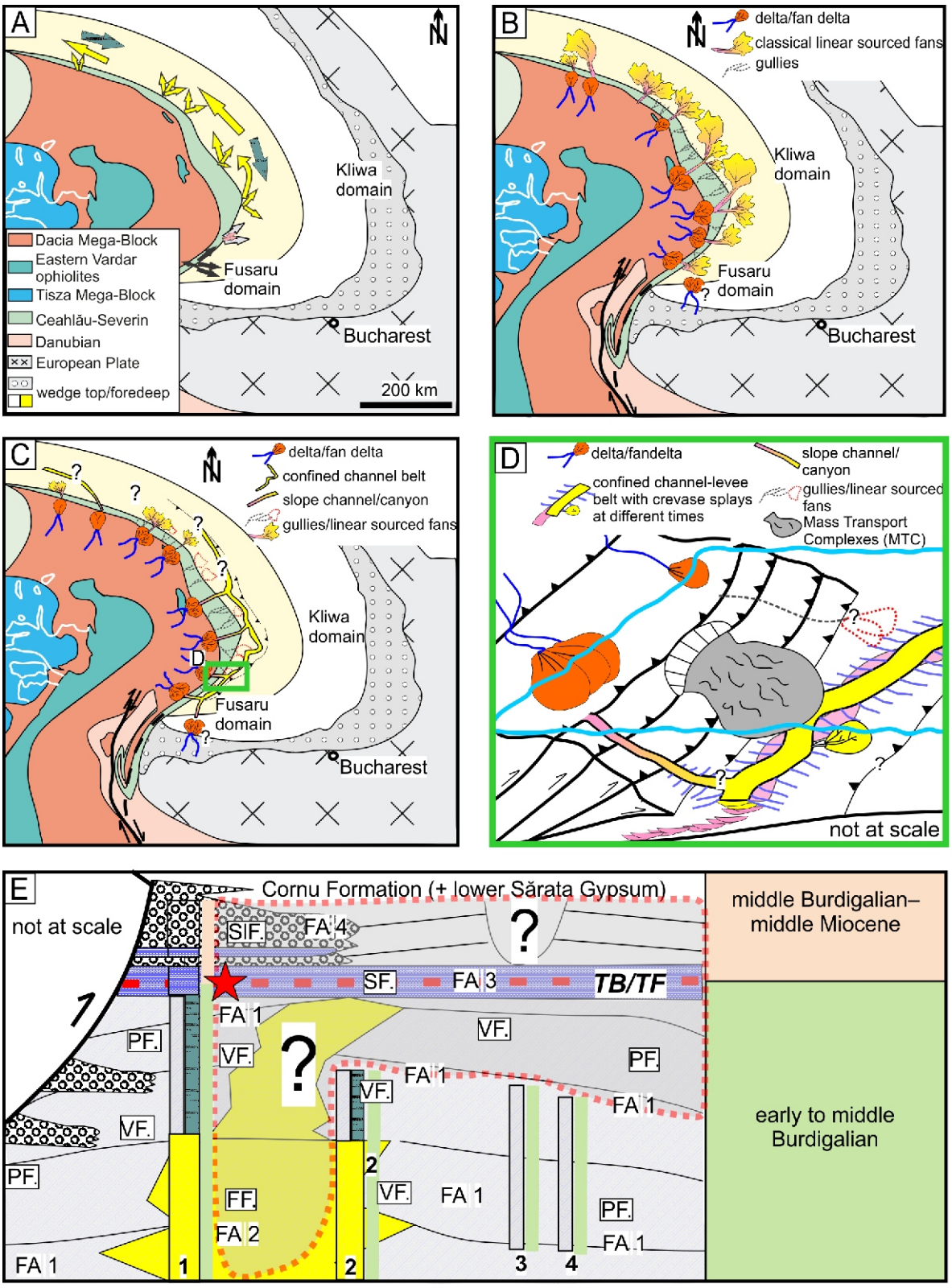

Fig. 7A – plotted palaeodirections on an early Miocene Carpathian foreland reconstruction (modified from Ustaszewski et al., 2008). Possible depositional environment interpretation: B – classical linear source gravitational flows – fan-shaped, that run approx. perpendicular to the basin axis; C – alternative interpretation with classical fans and a confined channels belt that run parallel to the orogen; D – close-up of the area of interest with continental/shallow marine sedimentation that feeds the confined channel-levee belt with crevasse-splay lobes. Also, large-scale Mass Transport Complexes were interpreted (see text for more details); E – hypothetical cross-section with the depositional environment interpretation based on logs and associated ages (PF. – Pucioasa Formation, VF. – Vineţişu Formation, PF. – Pucioasa Formation, SF. – Starchiojd Formation, SIF. – Slon Formation, FA.1 – Facies Association 1, TB/TF – Bătrani Tuff/Falcău Tuff). Red dotted light grey polygon represents the eroded area. Red star – U-Pb dated Bătrâni Tuff

clemenciae (e.g. around sample PN31–PN32; first occurrence in the Aquitanian M2 Zone) clearly demonstrate the Miocene age of the Vineţişu Formation. In the northern part of the section, corresponding to the Slon Formation (e.g. around sample PN40), the assemblage contains large planktonic foraminifera which were considered by Cicha et al. (1998) as ranging from the top of the early Miocene to mainly middle Miocene (Badenian): *Globigerina concinna, Globigerina diplostoma, Globigerinella regularis*. Other species, with larger ranges, but common in the Miocene, are present: *Globigerina bulloides, Globigerinella obesa, Globigerinita uvula*, *Globoturborotalita ouachitaensis* and *Tuborotalia quinqueloba*.

Although without specific biostratigraphic value, the calcareous benthic foraminifera from the dark grey mudstones of the Pucioasa Formation (Szabo, 2012; Fig. 3; samples PN20 to PN30) are of palaeoenvironmental importance. These are characteristic of outer neritic to bathyal settings (Culver, 1988; Leckie and Olson, 2003; Gooday and Jorissen, 2012), adapted to dysoxic conditions (*Brizalina alata, Br. pygmaea*, *Bolivina dilatata*, *Bol. molassica, Bol. liebusi*, *Bulimina elongata, Cassidulina margareta*, *Fursenkoina acuta*, *Globocassidulina oblonga*, *Nonionella stella, Oridorsalis umbonatus*, *Praeglobobulimina ovata, Pullenia bulloides, Valvulineria complanata, Virgulinella pertusa* etc.) or sometimes reflect oxic conditions on the substrate (*Amphimorphina hauerina*, *Elphidium grilli, E. hauerinum*, *E. reussi, Heterolepa dutemplei, Melonis pompilioides, Nodosaria elegantissima*, *Nonion commune* etc.).

PETROGRAPHY, ZIRCON U-Pb DATING AND TRACE ELEMENT COMPOSITION OF THE BĂTRÂNI TUFF

The Bătrâni Tuff is a fine-grained tuff within the Starchiojd Formation with up to 15–20% plagioclase, quartz and biotite of magmatic origin (Fig. 10A), the crystals of which are euhedral-subhedral, some being broken, with a narrow size distribution of 200–250 μm. The crystals are embedded in an altered (mostly argillitized) matrix that includes fossil moulds (Fig. 10A). The heavy minerals separated from the tuff are dominated by biotite, followed by zircon, apatite and ilmenite as magmatic crystals. The minerals suggest only minor reworking: zircon, apatite and phenocrysts have mostly euhedral or broken forms with no apparent chemical or mechanical abrasion; biotite is mostly fresh. The zircon grains have well developed magmatic zoning in cathodoluminescence images (Fig. 10B and Appendix 3). Data of *in situ* U-Pb dating is given in the Appendix 1.

We analysed 69 zircon crystal rim and 2 interior spots from which 61 give concordant results. A few spot analyses give older dates (interior: ~51 Ma, rims: ~189 Ma, ~240 Ma) whereas all others are Miocene. Two spot dates were excluded because of their high uncertainty. The 56 concordant Miocene dates range between 18.67 ±0.42 Ma and 17.09 ±0.27 Ma and they have a weighted mean age of 17.60 ±0.08 Ma with a Mean Squared Weighted Deviation (MSWD) value of 3.9 and three older outliers above 2 sigma uncertainty. The relatively high Mean Squared Weighted Deviation suggests more than one age component within the dates measured, therefore we calculated the low Mean Squared Weighted Deviation weighted mean age of the youngest age population, which is interpreted as the youngest crystallization age of the zircons. The youngest population with a weighted mean age of 17.41 ±0.06/0.27 Ma (MSWD = 1.5) is given by 32 dates. Therefore, 17.41 ±0.27 Ma (uncertainty also includes external errors) can be regarded as the closest age to the volcanic eruption represented by the zircon crystals. For the chemical characterization of the latest zircon crystallization domains we used the rim spots and excluded the relatively old and inclusion-contaminated data. Rim spots have 8250–10440 ppm Hf and 510–2727 ppm Y, Th/U ratio varies from 0.43 to 0.97 and U contents are between 384–1273 ppm. REE and Y contents show positive correlation with Th and U contents, while Hf shows negative correlation with Ti concentrations, which range between 1.5 and 6.8 ppm.

DISCUSSION

AGE INTERPRETATION

The biostratigraphy of the deposits studied needed reevaluation given the structural context and new radioisotopic age. As the interpreted age of the Bătrâni Tuff is 17.41 ±0.27 Ma, this regional lithological marker of the Starchiojd Formation (Ştefănescu et al., 1993; Figs. 3 and 5A1) must be placed in the middle Burdigalian (*sensu* Raffi et al., 2020).

The interval between samples PN21 and PN41 (Fig. 5A1) from the Fusaru and Slon formations (northern limb of the Moţăeni Anticline) represents the most continuous exposure (lithostratigraphically and chronologically) the section studied, ranging from the Burdigalian (NN2–NN4 Biozones) to middle Miocene, prior to the deposition of the middle Miocene Cornu Formation (Filipescu et al., 2020; Figs. 2A and 5A1). In the southern section, in the Miculeşti Syncline (Fig. 2A, B), the northern limb (Fig. 5A2) falls within the NN4 Biozone (correlating with the middle part of log 1) whereas the southern limb (Fig. 5A3) (or northern limb of the Diaconeşti-Vulcana Băi Anticline) was interpreted as falling within the NN2 Biozone. As the northern limb of the Miculeşti Syncline falls within the NN4 Biozone, we consider the equivalent upper part of the southern Miculeşti Syncline limb to fall also within the NN4 Biozone. Due to exposure gaps that affected the thickness measurements and some reverse faults (Fig. 5A3), the exact thickness of the NN4 Biozone in log 3 is difficult to assess, but it may be above sample PN8. To the west, in the Miculeşti Syncline (Fig. 2A), the younger Vineţişu and Starchiojd formations occur, therefore the NN4 Biozone for both limbs of the Miculeşti syncline from Pucioasa can be inferred. Nevertheless, in the Miculeşti syncline of the Pucioasa section, Ştefănescu et al. (1988) noted only Pucioasa deposits (Fig. 2A) although convolute sandstones, typical of the Vineţişu Formation, were observed (Fig. 6C). Regarding log 4 (Fig. 5A4) in the southern limb of the Diaconeşti-Vulcana Băi Anticline, the structural rationale suggests that it should have an lower–middle Burdigalian age (NN2–NN4 Biozones). The deposits belonging to the Starchiojd/Slon formations were not observed in logs 2, 3 and 4 (Fig. 5A2–A4). This may be due to lateral facies termination (i.e. Slon Formation) and erosion (Fig. 7E). Our results show that the age of the formations investigated along the Pucioasa section are younger than previously thought. The Fusaru and Pucioasa formations were previously considered as Oligocene (Ştefănescu et al., 1988; Melinte and Brustur, 2008), and the Vineţişu Formation as uppermost Oligocene to lower Burdigalian (NN2 Biozone; Mărunţeanu, 1999; Melinte and Brustur, 2008). Here we have an age model of not older than early Burdigalian (NN2 Biozone) and not younger than middle Burdigalian (NN4 Biozone) for the three formations. Even if the Starchiojd and Slon formations were interpreted as lower Burdigalian (NN2 Biozone; Mărunţeanu, 1999) we can expect an age ranging from middle Burdigalian to middle Miocene.

Interestingly, even if the calcareous nannoplankton zonation used for the 1:50,000 map of Ştefănescu et al. (1988) shows younger ages for the investigated formations, older ages were still assigned (Table 3).

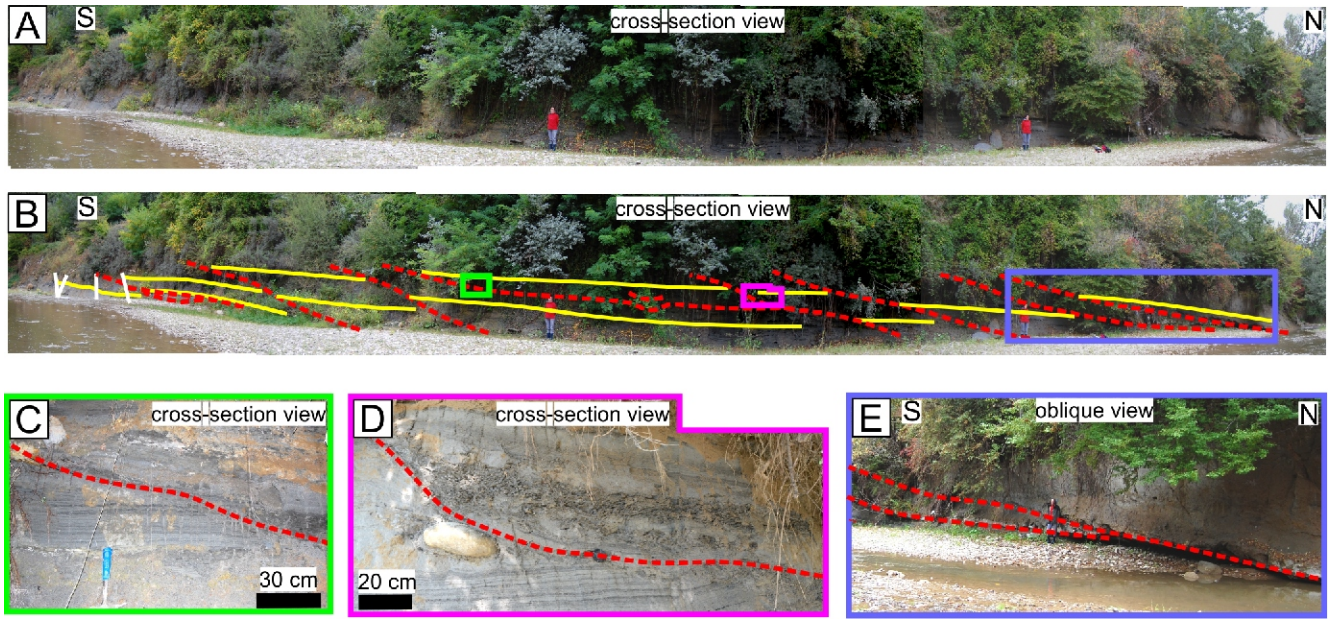

Fig. 8. Example of lateral offset cut and fill channel storeys (dashed red lines) with margin to axis bedsets (South to North) (Sprague et al., 2005)

A – uninterpreted image; **B** – Interpreted image; **C, D, E** – close-up of the erosional channel storey base

DEPOSITIONAL ENVIRONMENT INTERPRETATION

The four logs were arranged as they were mapped, from the anticline axial planes (Diaconeşti-Vulcana Băi, Moţăeni) outwards (Fig. 5A). This can be helpful in getting a better overview of the lateral sedimentary transition. We can interpret that the immediate southern Pucioasa Formation represents an overbank/levee sub environment (Fig. 5A3). It is difficult to deduce if this distributary channel – levee environment is part of a classical fan oriented perpendicularly to the basin axis (Posamentier and Walker, 2006; Fig. 7B) or an axial channel belt parallel to the basin (De Ruig and Hubbard, 2006; Fig. 7C). The measured palaeocurrents in the Fusaru Formation are to the ESE (Figs. 5B and 7A – pink arrows), similar to those measured in Pucioasa Formation (Conţescu et al., 1966; Fig. 7A – grey arrows) in the area. In the eastern part of the area investigated Conţescu et al. (1966) noted that the distance covered by

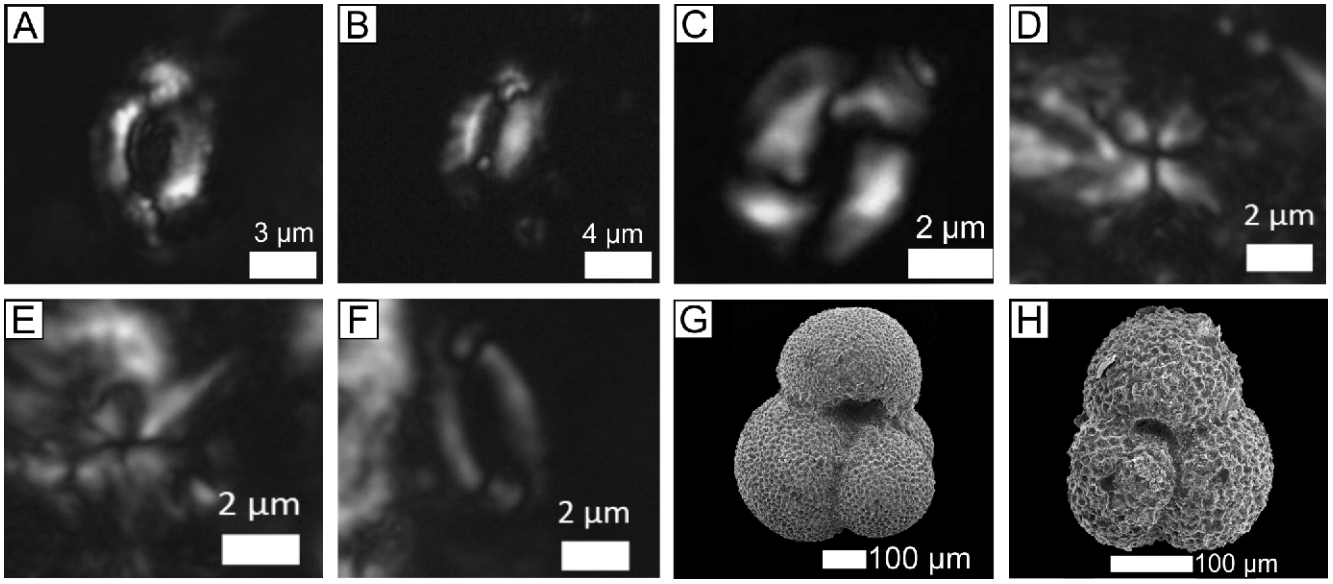

Fig. 9. Representative Miocene biostratigraphic markers

A–F calcareous nannoplankton, G, H foraminifera: **A** – *Helicosphaera ampliaperta* (PN5); **B** – *Helicosphaera scissura* (PN18); **C** – *Reticulophaenestra pseudoumbilicus* (PN18); **D** – *Sphenolithus heteromorphus* – same as **E**, different orientation (PN14); **F** – *Helicosphaera walbersdorfensis* (PN30); **G** – *Trilobatus quadrilobatus*.; **H** – *Trilobatus subsacculifer*

Table 2

Calcareous nannoplankton fossils found within the samples analysed

Samples/Calcareous nannoplankton	PN 20	PN 19	PN 18	PN 17	PN 16	PN 1	PN 2	PN 3	PN 4	PN 5	PN 6	PN 7	PN 8	PN 9	PN 10	PN 11	PN 15	PN 14	PN 13	PN 12	PN 21	PN 22	PN 23*	PN 24	PN 25	PN 26	PN 27	PN 28	PN 29	PN 30	PN 31	PN 32	PN 33	PN 34	PN 35	PN 36	PN 37	PN 38	PN 39	PN 40	PN 41
Braarudosphaera bigelowii		x								x	x	x													x	x	x	x						x					
Clausicoccus fenestratus																		x							x		x				x			x					
Coccolithus pelagicus	x	x	x					x		x	x	x		x			x	x	x	x	x	x	x	x	x	x	x	x	x	x	x	x	x	x	x		x		
Coccolithus miopelagicus																		x	x					x	x			x	x	x			x	x						
Coronocyclus nitescens					x							x								x										x										
Cyclicargolithus abisectus		x			x													x							x			x	x	x	x			x	x					
Cyclicargolithus floridanus	x	x	x					x		x	x	x		x			x	x	x	x	x	x	x	x	x	x	x	x	x	x	x	x	x	x		x	x		
Discoaster deflandrei											x													x	x				x		x		x	x			x		x	
Discoaster cf. *druggii*																											x	x												
Helicosphaera ampliaperta								x		x		x		x			x	x	x	x			x	x	x			x	x	x	x		x	x	x	x				
Helicosphaera carteri		x						x			x		x					x		x		x	x	x	x	x	x	x	x	x	x	x	x	x	x		x			
Helicosphaera euphratis			x							x	x	x																x			x	x		x						
Helicosphaera intermedia											x	x		x						x			x	x				x	x		x			x						
Helicosphaera mediterranea																		x														x								
Helicosphaera recta	x																													x										
Helicosphaera scissura	x	x						x		x	x							x	x		x	x		x	x	x	x	x	x	x	x		x	x	x					
Helicosphaera walbersdorfensis																		x												x			x							
Pontosphaera multipora		x	x					x		x	x	x										x		x	x	x	x	x	x	x	x	x	x	x		x				
Reticulofenestra bisecta	x	x	x	x						x	x	x	x				x	x	x		x				x		x	x	x	x	x	x		x	x	x	x				
Reticulofenstra daviesii	x	x	x									x						x							x			x	x	x	x		x	x	x	x				
Retecapsa haqii	x	x	x					x	x	x	x	x	x				x	x	x		x	x	x	x	x	x	x	x	x	x		x		x	x	x	x		x	
Reticulofenestra minuta	x		x					x		x	x	x		x			x		x	x	x	x	x	x	x	x	x	x	x	x			x	x	x	x			
Reticulofenestra producta		x		x													x		x				x					x			x	x		x	x		x			
Reticulofenestra pseudoumbilicus	x	x	x	x				x		x	x	x	x	x			x	x	x	x	x	x	x	x	x	x	x	x	x	x	x	x	x	x	x	x	x		x	
Reticulofenestra stavensis																			x			x			x			x								x				
Sphenolithus conicus												x												x		x		x	x	x	x	x	x	x		x				
Sphenolithus dissimilis																												x	x			x					x			
Sphenolithus disbelemnos																									x															
Sphenolithus belemnos																												x					x	x						
Sphenolithus heteromorphus																		x																						
Sphenolithus moriformis								x		x		x		x				x	x	x	x		x	x	x	x	x	x	x	x	x	x	x	x	x	x		x		
Sphenolithus procerus																	x		x																					
Triquetrorhabdulus carinatus																					x				x															
Umbilicosphaera rotula												x		x										x										x						
Umbilicosphaera jafari												x		x																				x						

Sterile

Sterile

Sterile

* – sample PN23 taken from a mudstone rip up clast

the coarse-grained longitudinal flow deposits of the Fusaru Formation was ~200–250 km. They considered that the flows started in the area of ECBZ between Ploeşti and Buzău (Figs. 1B and 7A) and went northwards parallel to the fold and thrust belt along what is today the Eastern Carpathians. This distance in present day configuration covers almost all of the Eastern Carpathians (Fig. 1B). West of the area investigated, in the Getic Depression (Fig. 1B), Fusaru-like slope coarse-grained siliciclastic deposits (Roban, 2008; Corbi and Cheia formations) were described as having a dominant SE-wards palaeocurrent direction (black arrows; Figs. 1B and 7A) by Jipa (1982, 1994 *fide* Roban, 2008). However, this could have fed some older Fusaru Formation, that now lies at depth in the area investigated (Fig. 7C, D). As the formations from the study area are younger than previously interpreted, that constrast with the rest of the Getic – ECBZ – Eastern Carpathians stratigraphy, we consider that a regional study is necessary for age re-evaluation. Nevertheless, the existing palaeocurrent data can be used, as regardless of age it shows dominant eastwards/northwards longitudinal (Jipa, 1966) current flow. As the palaeoflow in the area of study is to the east, and appears to be parallel to the orogen, we consider the Pucioasa and Fusaru formations as part of an axial channel levee belt (Hubbard et al., 2008; Fig. 7D) that originated in the west (Getic Depression). It may have flowed north-eastwards, eastwards (Fig. 7A) and perhaps continued towards the Eastern Carpathians. Probably it was also fed by transverse flows from the hinterland (Hubbard et al., 2008) coexisting with classical transverse fan environments (Conţescu et al., 1966; Jipa, 1966; Fig. 7C). It is difficult to say whether the axial channel levee belt was continuous for hundreds of kilometres and extended across all of the Eastern Carpathians or whether was discontinuous. The characteristic convolute sandstones of the Vineţişu Formation present in the lower and middle part of log 1 disappear upwards (Figs. 2A, 5A1 and 7E) into beds characteristic of the Pucioasa Formation. Also, in the northern limb of the Miculeşti Syncline, many convolute sandstones developed in what was interpreted as Pucioasa Formation (Ştefănescu et al., 1988). These sandstones may be equivalent to the convolute sandstones from the lower-middle part of the Vineţişu Formation in log 1. We interpret the Fusaru channels as having migrated laterally (Fig. 7E), for instance between the areas of log 1 and log 2 (eroded today). Therefore, the Vineţişu and Pucioasa formations are lateral equivalents, related to a channel overbank/levee sub-environment where the Pucioasa Formation was distal in relation to the Vineţişu Formation. Only 3 qualitative palaeoflow measurements were made for some asymmetrical ripples around samples PN29–PN30 and these have a roughly eastwards direction (no bed tilt correction). Conţescu et al. (1966) plotted some south and south-west palaeoflows (green arrows; Figs. 1B and 7A) for the Vineţişu Formation (in the Eastern Carpathians area) but did not record from where in the formation the measurements were taken. The only westwards-directed palaeoflows observed (no tectonic tilt correction) relate to ripples from the Bătrâni Tuff within the restricted Starchiojd Formation (Fig. 6Q). Ştefănescu et al. (1993) considered the lower Miocene tuffs of the ECBZ as deposited by bottom currents. As the compression migrated in a foreland direction, the Fusaru channels and associated formations migrated laterally (Fig. 7E). This can be seen through the presence of the very thick Slon Formation (Fig. 5A1) related to the active compressional tectonics. This facies is diachronous (Ştefănescu et al., 1988; Răbăgia et al., 2011) given its presence elsewhere within the Vineţişu and Cornu formations (Olteanu, 1952; Ştefănescu, 1995) and probably follows the movement of the thrusts. Similar synkinematic deposits have been documented in the Ukrainian Carpathians (Hnylko, 2014). The ~100-m-thick massive to convolute sandstones with fine conglomerates described by Ştefănescu (1995) somewhere towards the hinterland should not be interpreted as Slon Formation as the latter is a cohesive debrite while the sandstones relate to high-density gravitational flows. As the younger shallow marine piggyback deposits of the Valea Lungă Syncline are considered middle Miocene (Bercea et al., 2016; Filipescu et al., 2020; Figs. 2A,B and 5A4), then at the time of deposition of the deep marine exposures investigated, the lateral shallow marine equivalent was situated somewhere towards the hinterland.

ORIGIN OF THE BĂTRÂNI TUFF

Early Miocene silicic pyroclastic rocks and volcanic ash-bearing strata are known at many localities in the Carpathian-Pannonian region and also in its surroundings as both proximal and distal facies (e.g., Alexandrescu et al., 1981, 1994; Ştefănescu et al., 1993; Szakács et al., 2012; de Leeuw et al., 2013; Lukács et al., 2015, 2018, 2021; Rocholl et al., 2018; Rybár et al., 2019; Brlek et al., 2020; Sant et al., 2020; Danisik et al., 2021; Šarinová et al., 2021). The distal pyroclastic intercalations (usually tuffs) have a great importance not only in dating sedimentary sections, but also in revealing the nature of the silicic explosive volcanic activity (areal coverage, volume and explosivity) of that time. Lukács et al. (2018) identified four main early Miocene ignimbrite-forming explosive eruptions in the Bükkalja Volcanic Field, northern Hungary; these are the Csv-2 ignimbrite at 18.2 ±0.3 Ma, the Eger ignimbrite at 17.5 ±0.3 Ma, the Mangó ignimbrite at 17.065 ±0.014 Ma and the Bogács ignimbrite at 16.816 ±0.059 Ma. Recently, Karátson et al. (2022) and Brlek et al. (2023) refined the age of the Eger eruption event to 17.3 Ma and the Csv-2 (named as Wind/Kalnik) eruption to 18.1 Ma with <100 ky uncertainties. The thick Bătrâni Tuff from the ECBZ represents the product of one such eruption, which provides indication of a possible large explosive volcanic event. It was correlated by Frunzescu (2013), based on lithostratigraphy, with the Falcău Tuff (Alexandrescu et al., 1981) of the Eastern Carpathians

Table 3

Reinterpreted calcareous nannoplankton from Ştefănescu et al. (1988)

Stratigraphy based on Ştefănescu et al. (1988)			Age reinterpretation based on calcareous nannoplankton	
Slon Formation	Starchiojd Formation	lower Miocene	*Sphenolithus heteromorphus*	not older than Burdigalian (NN4 Biozone)
	Vineţişu Formation	Oligo–lower Miocene	*Sphenolithus belemnos*	Burdigalian (NN3 Biozone)
Pucioasa and Fusaru formations		Oligocene	*Helicosphaera ampliaperta*	not older than Burdigalian (NN2 Biozone)

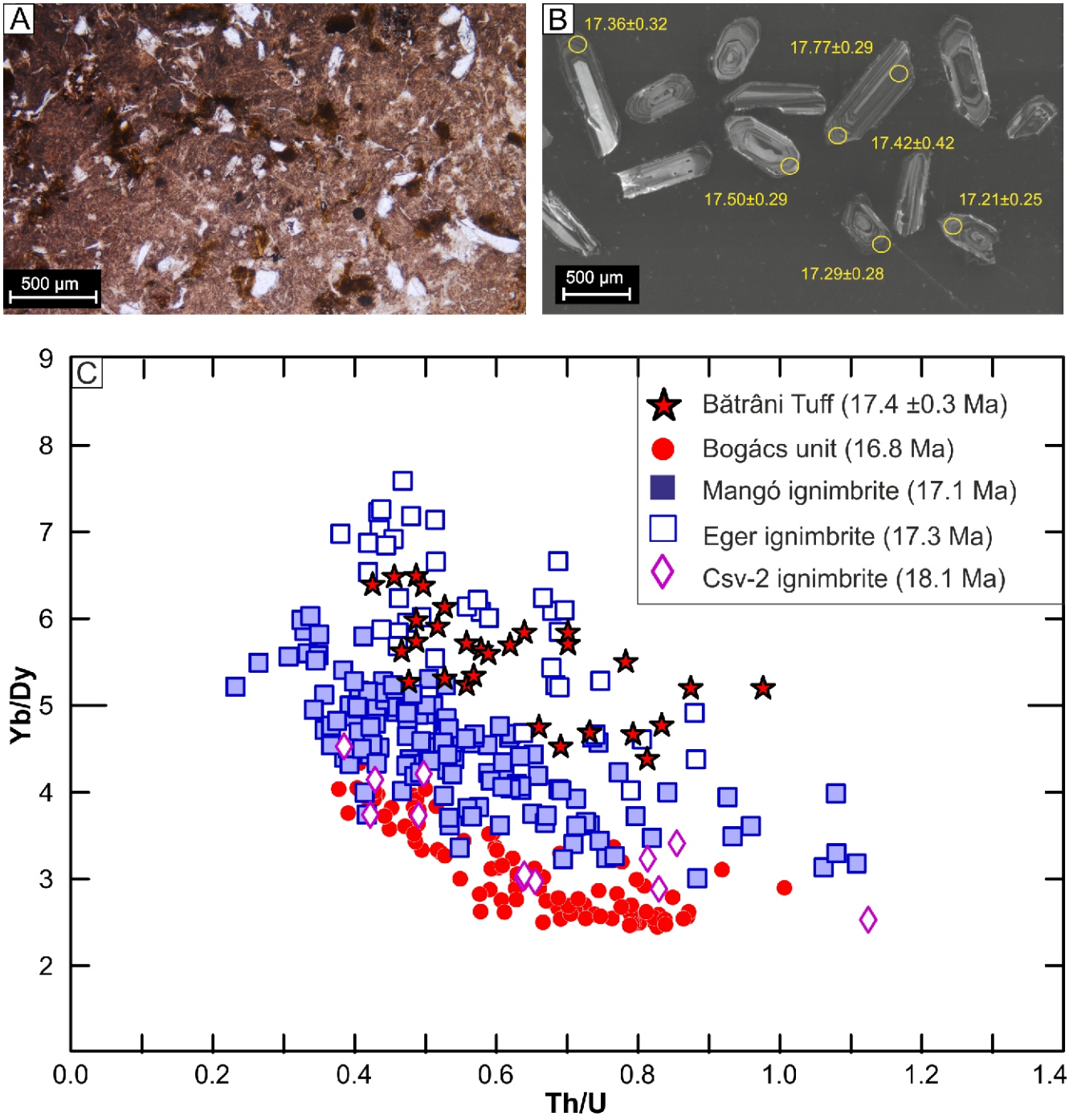

Fig. 10A – optical microscopic image (4x) of the Bătrâni Tuff showing angular crystals (feldspar, quartz, biotite), fossil fragments in altered matrix; B – cathodoluminescence images of zircon crystals separated from the tuff with spots (30 µm) of Laser Ablation Inductively Coupled Plasma Mass Spectrometry (LA-ICP-MS) analyses. Ages are in millions of years; C – zircon trace element ratios discriminating the lower Miocene main ignimbrite units of the Bükkalja Volcanic Field after Lukács et al. (2021). The Bătrâni Tuff zircons show similar trace element ratios to those of the Eger ignimbrite

(Fig. 3). The homogeneous grain (phenocryst) size distribution, mineral assemblage, the freshness and un-abraded character of the magmatic minerals of the Bătrâni Tuff sample studied suggest a rapid and relatively short re-sedimentation route, presumably by low-density turbidity currents/marine bottom currents after fall deposition. The source of the pyroclastic material can be inferred using combined geochronological and geochemical correlation (e.g., Lowe, 2011; Lowe et al., 2017; Pearce et al., 2020; Lukács et al., 2021; Prentice et al., 2022). The age of the tuff within uncertainty can be correlated with the ~17.3 Ma Eger ignimbrite-forming eruption of the Bükkalja Volcanic Field. The Eger ignimbrite is a ~30 m thick silicic lapilli tuff proximally (i.e. in the Bükkalja Volcanic Field) with a similar main mineral assemblage (quartz, plagioclase, biotite). In the case of the Bătrâni Tuff studied, the juvenile glass fragments are not suitable for chemical characterization and correlation due to their severe alteration. Lukács et al. (2021) showed that zircon trace element compositions can be effectively used to

correlate the main pyroclastic units of the Bükkalja Volcanic Field (Fig. 1A) with their distal counterparts and suggested that this geochemical correlation technique could be powerful in case of altered pyroclastic deposits. In bivariate trace element and trace element ratio diagrams a striking similarity can be observed between the zircons of the Bătrâni Tuff and those of the Eger ignimbrite (Fig. 10C). The distinct chemical composition of the Eger ignimbrite zircons among the early Miocene ignimbrites of the Bükkalja Volcanic Field is best visualized on the Th/U versus Yb/Dy diagram (Lukács et al., 2021). Zircons of the Bătrâni Tuff have a high Yb/Dy ratio for a given Th/U ratio (Fig. 10C) as shown also by zircon crystals in the Eger ignimbrite of the Bükkalja Volcanic Field. They share this distinctive character among the early Miocene pyroclastic rocks (Fig. 10C). Thus, the similar phenocryst assemblage, zircon U-Pb age and zircon chemistry all suggest that the Bătrâni Tuff as a distal product of the 17.3 Ma Eger eruption.

The pyroclastic suite at Ipolytarnóc (North Hungary), ~75 km away from the proximal BVF deposit, also has a similar zircon U-Pb and $^{40}Ar/^{39}Ar$ age and zircon trace element composition to the Eger ignimbrite as shown by Lukács et al. (2021), Šarinová et al. (2021) and Karátson et al. (2022). Brlek et al. (2023) identified the Eger eruption-related ignimbrite in the Mt. Kalnik (Croatia) and fall deposits in the Sinj Basin (Croatia), based on zircon U-Pb dating, glass and zircon geochemistry. Possible distal counterparts of the Eger eruption were proposed by Lukács et al. (2018) west from the Pannonian basin, in the Northern Alpine Foreland. We propose here that the Bătrâni Tuff may be another distal deposit of this eruption event and the first example demonstrating that pyroclastic fall occurred also east-southeast of the Bükkalja Volcanic Field, the ash being deposited in a deep marine environment.

CONCLUSIONS

This integrated structural, sedimentological and biostratigraphic study, coupled with zircon U-Pb dating, provides better constraints on the age of the stratigraphic sequence investigated. The Pucioasa, Fusaru and Vineţişu formations have an early to middle Burdigalian age (NN2-NN4 biozones). The age of a regional lithological marker of the Starchiojd Formation was obtained by U-Pb dating of the Bătrâni Tuff, resulting in an age of 17.41 ±0.27 Ma, which falls within the middle Burdigalian. The re-interpretation of older calcareous nannoplankton data from Ştefănescu et al., (1988) also shows a Burdigalian age (NN2–NN4 Biozones).

The deposits studied are interpreted as a longitudinal stacked channels belt (Fusaru Formation) with associated levee/overbank (Pucioasa, Vineţişu formations) deposits which are lateral equivalents, sourced from the west. They migrated laterally as the compression propagated towards the foreland. This propagation can also be interpreted through the presence of the diachronous Mass Transport Complexes of the Slon Formation, which was formed through the collapse of the upper shelf due to hinterland nappe stacking. The Bătrâni Tuff in the ECBZ with its Eastern Carpathians correlative the Falcău Tuff (Frunzescu, 2013) may be a distal counterpart of one of the largest eruptions identified in the Bükkalja Volcanic Field, Hungary, based on their similar zircon U-Pb age and trace element composition. In this case, the Bătrâni Tuff is the first identified pyroclastic fall deposit of the 17.3 Ma Eger eruption event, several hundred kilometres east-southeastwards of the Bükkalja Volcanic Field.

The formations exposed in our study area were most likely subsequently deformed during the intra-Burdigalian/Badenian –Sarmatian and the Wallachian phases. The former is most likely associated with the earlier NNW–SSE-trending thrust, while the latter is associated with E–W to WSW–ENE-trending contractional structures. This later event is also associated with NNW-SSE-trending dextral faults (and associated Riedel shear structures) acting as tear faults which partitioned the deformation in the area.

Nevertheless, regional studies including source area analysis, more palaeocurrent data measurements integrated within a depositional environment interpretation and detailed structural analysis is required, in order to reach better understanding of the evolution of lateral depositional environments along this Carpathians internal foredeep/wedge top setting.

Acknowledgements. R. Bercea wants to thank his family for having the patience to stay with him while logging the Pucioasa section and also L. Todoran for English language corrections. C. Krézsek, V. Barbu, R. Olaru, E. Săsăran, S. Botond, G. Iordache and L. Zaharia are thanked for early discussion regarding the Pucioasa section. D.M. Tămaş thanks the UEFISCDI PN-III-P1-1.1-PD-2021-0165 no PD17/2022 for the financial support. U-Pb dating was supported by the National Research, Development and Innovation Office – NKFIH (Hungary) within the FK OTKA project (No. 131869). The work of R. Lukács was supported by the Bolyai János Research Fellowship. Three anonymous reviewers are thanked for carefully reading the manuscript and making suggestions that helped to significantly improve this article.

REFERENCES

Abreu, V., Sullivan, M., Pirmez, C., Mohrig, D., 2003. Lateral accretion packages (LAPs): an important reservoir element in deep water sinuous channels. Marine and Petroleum Geology, **20**: 631–648.

Alexandrescu, G., Brustur, T., Matei, V., Antonescu, A., 1981. On some cinerites from the central and northern part of the Eastern Carpathians (in Romanian). Dări de seamă ale Institutului Geologic şi Geofizică, **68**: 69–90.

Alexandrescu, G., Frunzescu, D., Brustur, T., 1994. The Vălenii de Munte tuff – petrographic and stratigraphic significance (in Romanian). Studii şi cercetări de geologie, **39**: 51–57.

Allmendinger, R.W., Cardozo, N., Fisher, D., 2012. Structural Geology Algorithms: Vectors and Tensors in Structural Geology. Cambridge University Press, Cambridge.

Amadori, M. L., Belayouni, H., Guerrera, F., Martin-Martin, M., Martin-Rojas, I., Miclăuş, C., Raffaelli, G., 2012. New data on the Vrancea Nappe (Moldavidian Basin, Outer Carpathian Domain, Romania): paleogeographic and geodynamic reconstructions. International Journal of Earth Sciences, **101**: 1599–1623.

Angelier, J., 1990. Inversion of field data in fault tectonics to obtain the regional stress III: a new rapid direct inversion method by analytical means. Geophysical Journal International, **103**: 363–376.

Bădescu, D., 2005. Tectono-sratigraphic evolution of the Eastern Carpathians during Mesozoic and Cenozoic (in Romanian). Ed. Economică, Bucharest.

Balintoni, I., Balica, C., Ducea, M., Han, H., 2014. Peri-Gondwanan terranes in the Romanian Carpathians: a review of their spatial distribution, origin, provenance, and evolution. Geosciences Frontiers, **5**: 395–411.

Belayouni, H., Staso, A., Guerrera, F., Martin–Martin, M., Miclăuş, C., Serrano, F., Tramontana, M., 2007. Stratigraphic and geochemical study of the organic-rich black shales in the Tarcău Nappe of the Moldavidian Domain (Carpathian Chain, Romania). International Journal of Earth Sciences, **98**: 157–176.

Beldean, C., Filipescu, S., Bălc, R., 2012. Paleoenvironmental and biostratigraphic data for the Early Miocene of the North-Western Transylvanian Basin based on planktonic foraminifera. Carpathian Journal of Earth and Environmental Sciences, **7**: 171–184.

Bercea, R., Bălc, R., Filipescu, S., Zaharia, L., Pop, S., 2016. Middle Miocene micropaleontological and sedimentary aspects within a piggy-back basin, Pucioasa section, Carpathian Bend Zone, Romania. AAPG European Regional Conference and Exhibition, Bucharest, Abstract Book, 50.

Boesiger, T.M., De Kaenel, E., Bergen, J.A., Browning, E., Blair, S.A., 2017. Oligocene to Pleistocene taxonomy and stratigraphy of the genus *Helicosphaera* and other placolith taxa in the circum North Atlantic Basin. Journal of Nannoplankton Research, **37**: 145–175.

Bouma, A.H., 1962. Sedimentology of Some Flysch Deposits: A Graphic Approach to Facies Interpretation. Elsevier, Amsterdam.

Bown, P.R., Young, J.R., 1998. Techniques. In: Calcareous Nannofossil Biostratigraphy (ed. P.R. Bown): 16–28. Kluwer, Dordrecht.

Brlek, M., Kutterolf, S., Gaynor, S., Kuiper, K., Belak, M., Brcic, V., Holcova, K., Wang, K.L., Bakrac, K., Hajek – Tadesse, V., Misur, I., Horvat, M., Suica, S., Schaltegger, U., 2020. Miocene syn-rift evolution of the North Croatian Basin (Carpathian–Pannonian Region): new constraints from Mts. Kalnik and Požeška gora volcaniclastic record with regional implications. International Journal of Earth Sciences, **109**: 2775–2800.

Brlek, M., Tapster, S.R., Schindlbeck-Belo, Gaynor, J.S.P., Kutterolf, S., Hauff, F., Georgiev, S.V., Trinajstić, N., Šuica, S., Brčić, V., Wang, K-L., Lee, H-Y., Beier, C., Abersteiner, A.B., Mišur, I., Peytcheva, I., Kukoč, D., Németh, B., Trajanova, M., Balen, D., Guillong, M., Szymanowski, D., Lukács, R., 2023. Tracing widespread Early Miocene ignimbrite eruptions and petrogenesis at the onset of the Carpathian-Pannonian Region silicic volcanism. Gondwana Research, **116**: 40–60.

Bucur, I., 1966. Contributions to the understanding of Oligocene breccias from Siriu valley (Buzău Mountains). Dări de seamă ale Şedinţelor Institutului de Geologie şi Geofizică, **53**: 476–483.

Cardozo, N., Allmendinger, R.W., 2013. Spherical projections with OSXStereonet. Computers and Geosciences, **51**: 193–205.

Carne, R.C., Little, T.A., 2012. Geometry and scale of fault segmentation and deformational bulging along an active oblique-slip fault (Wairarapa fault, New Zealand). GSA Bulletin, **124**: 1365–1381.

Cicha, I., Rögl, F., Rupp, C., Čtyroka, J., 1998. Oligocene-Miocene foraminifera of the Central Paratethys. Abhandlungen der Senckenbergischen Naturforschenden Gesellschaft, **549**: 1–325.

Collinson, J., Mountney, N., Thompson, D., 2006. Sedimentary Structures, third edition. Terra Publishing, Harpenden.

Conţescu, L., Jipa, D., Mihăilescu, N., Panin, N., 1966. The internal Paleogene flysch of the Eastern Carpathians: paleocurrents, source areas and facies significance. Sedimentology, **7**: 307–321.

Culver, S.J., 1988. New foraminiferal depth zonation of the northwestern Gulf of Mexico. Palaios, **3**: 69–85.

Danisik, M., Ponomareva, V., Portnyagin, M., Popov, S., Zastrozhnov, A., Kirkland, C. L., Evans, N. J., Konstantinov, E., Hauff, F., Garbe – Schonberg, D., 2021. Gigantic eruption of a Carpathian volcano marks the largest Miocene transgression of Eastern Paratethys. Earth and Planetary Science Letters, **563**: 116890.

De Leeuw, A., Filipescu, S., Maţenco, L., Krijgsman, W., Kuiper, K., Stoica, M., 2013. Paleomagnetic and chronostratigraphic constraints on the Middle to Late Miocene evolution of the Transylvanian Basin (Romania): implications for Central Paratethys stratigraphy and emplacement of the Tisza–Dacia plate. Global and Planetary Change, **103**: 82–98.

De Ruig, J.M., Hubbard, S., 2006. Seismic facies and reservoir characteristic of a deep – marine channel belt in the Molasse foreland basin, Puchkirchen Formation, Austria. AAPG Bulletin, **90**: 735–752.

Delvaux, D., Moeys, R., Stapel, G., Petit, C., Levi, K., Miroschnichenko, A., Ruzhich, V., San'kov, V., 1997. Paleostress reconstructions and geodynamics of the Baikal region, Central Asia, Part 2. Cenozoic rifting. Tectonophysics, **282**: 1–38.

Ducea, M.N., Negulescu, E., Profeta, L., Săbău, G., Jianu, D., Petrescu, L., Hoffman, D., 2016. Evolution of the Sibişel Shear Zone (South Carpathians): a study of its type locality near Răşinari (Romania) and tectonic implications. Tectonics, **35**: 2131–2157.

Duranti, D., Hurst, A., 2004. Fluidization and injection in the deep-water sandstones of the Eocene Alba Formation (UK North Sea). Sedimentology, **51**: 503–529.

Filipescu, S., Silye, L., 2008. New Paratethyan biozones of planktonic foraminifera described from the Middle Miocene of the Transylvanian Basin. Geologica Carpathica, **59**: 537–544.

Filipescu, S., Tămaş, D. M., Bercea, R. I., Tămaş, A., Bălc, R., Ţabără, D., Bindiu-Haitonic, R., Silye, L., Auer, A., Krezsek, C., Schleder, Z., Săsăran, E., 2020. Biostratigraphic re-evaluation of the lower to middle Miocene successions in the Eastern Carpathians: a case study related to the oil field of the Diapir Fold Zone, Romania. Geological Quarterly, **64** (3): 781–800.

Fongngern, R., Olariu, C., Steel, R., Mohrig, D., Krezsek, C., Hess, T., 2018. Subsurface and outcrop characteristic of fluvial – dominated deep – lacustrine clinoforms. Sedimentology, **65**: 1447–1481.

Frunzescu, D., 2013. The Miocene from the Southern part of the Eastern Carpathians. Sulphatic evaporitic megasequences (in Romanian). Oil – Gas University Publishing, Ploieşti.

Funk, J., Slatt, R., Pyles, D., 2012. Quantification of static connectivity between deep-water channels and stratigraphically adjacent architectural elements using outcrop analogs. AAPG Bulletin, **96**: 277–300.

Gooday, A.J., Jorissen, F.J., 2012. Benthic foraminiferal biogeography: controls on global distribution patterns in deep-water settings. Annual Review of Marine Science, **4**: 237–262.

Grunert, P., Soliman, A., Coric, C., Scholger, R., Harzhauser, M., Piller, W.E., 2010. Stratigraphic re-evaluation of the stratotype for the regional Ottnangian stage (Central Paratethys, middle Burdigalian). Newsletter on Stratigraphy, **44**: 1–16.

Hippolyte, J.C., Săndulescu, M., 1996. Paleostress characterization of the 'Wallachian' phase in its type area, southeastern Carpathians. Tectonophysics, **263**: 235–249.

Hnylko, O., 2014. Olistostromes in the Miocene salt-bearing folded deposits at the front of the Ukrainian Carpathian orogen. Geological Quarterly, **58** (3): 381–392.

Hohenegger, J., Rögl, F., Coric, S., Pervesler, P., Lirer, F., Roetzel, R., Scholger, R., Stingl, K., 2009. The Styrian Basin: key to the Middle Miocene (Badenian/Langhian) Central Paratethys transgressions. Austrian Journal of Earth Sciences, **102**: 102–132.

Hubbard, S.M., Romans, B.W., Graham, S.A., 2008. Deep-water foreland basin deposits of the Cerro Toro Formation, Magallanes basin, Chile: architectural elements of a sinuous basin axial channel belt. Sedimentology, **55**: 1333–1359.

Hubbard, S.M., De Ruig, J.M., Graham, S.A., 2009. Confined channel – levee complex development in an elongated deep–center: Deep–water Tertiary strata of the Austrian Molasse basin. Marine and Petroleum Geology, **26**: 85–112.

Jipa, D., 1966. Relationship between longitudinal and transversal currents in the Paleogene of the Tarcău Valley (Eastern Carpathians). Sedimentology, **7**: 299–305.

Jobe, Z.R., Lowe, D.R., Morris, W.R., 2011. Climbing ripples successions in turbidite systems: depositional environments, sedimentation rates and accumulation times. Sedimentology, **59**: 867–898.

Joja, T., 1952. The geological structure of the marginal flysch from Suha Mică and Suha Mare valleys (in Romanian). Dări de Seamă ale Institutului Geologic, **36**: 12–23.

Kamb, W.B., 1959. Ice petrofabric observations from Blue Glacier, Washington, in relation to theory and experiment. Journal of Geophysical Research, **64**: 1891–1909.

Karátson, D., Biró, T., Portnyagin, M., Kiss, B., Paquette, J.-L., Cseri, Z., Hencz, M., Németh, K., Lahitte, P., Márton, E., Kordos, L., Józsa, S., Hably, L., Müller, S., Szarvas, I., 2022. Large-magnitude (VEI ? 7) 'wet' explosive silicic eruption preserved a Lower Miocene habitat at the Ipolytarnóc Fossil Site, North Hungary. Scientific Reports, **12**: 9743.

Kim, Y.S., Sanderson, D.J., 2006. Structural similarity and variety at the tips in a wide range of strike-slip faults: a review. Terra Nova, **18**: 330–344.

Kováč, M., Hudáčková, N., Halásová, E., Kováčová, M., Holcová, K., Oszczypko-Clowes, M., Báldi, K., Less, G., Nagymarosy, A., Ruman, A., Klučiar, T., Jamrich, M., 2017. The Central Paratethys paleoceanography: a water circulation model based on microfossil proxies, climate, and changes of depositional environment. Acta Geologica Slovaca, **9**: 75–114.

Kraütner, H.G., Bindea, G., 2002. Structural units in the pre - Alpine basement of the Eastern Carpathians. Geologica Carpathica, **53**: 143–146.

Krézsek, C., Lăpădat, A., Maţenco, L., Arnberger, K., Barbu, V., Olaru, R., 2013. Strain partitioning at orogenic contacts during rotation, strike–slip and oblique convergence: Paleogene Early Miocene evolution of the contact between the South Carpathians and Moesia. Global and Planetary Change, **103**: 63–81.

Leckie, R.M., Olson, H.C., 2003. Foraminifera as proxies of sea-level change on siliciclastic margins. SEPM Special Publication, **75**: 5–19.

Leever, K.A., Maţenco, L., Bertotti, G., Cloetingh, S., Drijkoningen, G., 2006. Late Orogenic vertical movements in the Carpathian Bend Zone - seismic constraints on the transition zone from orogen to foredeep. Basin Research, **18**: 521–545.

Lowe, D.J., 2011. Tephrochronology and its application: a review. Quaternary Geochronology, **6**: 107–153.

Lowe, D.J., Pearce, N.J.G., Jorgensen, M.A., Kuehn, S.C., Tryon, C.A., Hayward, C.L., 2017. Correlating tephras and cryptotephras using glass compositional analyses and numerical and statistical methods: review and evaluation. Quaternary Science Reviews, **175**: 1–44.

Lowe, D.R., 1982. Sediment gravity flows II. Depositional models with special reference to the deposits of high-density turbidity currents. Journal of Sedimentary Petrology, **52**: 279–297.

Lowe, D.R., Guy, M., 2000. Slurry-flow deposits in the Britannia Formation (Lower Cretaceous), North Sea: a new perspective on the turbidity current and debris flow problem. Sedimentology, **47**: 31–70.

Lukács, R., Harangi, S., Bachmann, O., Guillong, M., Danišík, M., Buret, Y., Von Quadt, A., Dunkl, I., Fodor, L., Sliwinski, J., Soós, I., Szepesi, J., 2015. Zircon geochronology and geochemistry to constrain the youngest eruption events and magma evolution of the Mid-Miocene ignimbrite flare - up in the Pannonian Basin, eastern central Europe. Contributions to Mineralogy and Petrology, **170**: 52.

Lukács, R., Harangi, S., Guillong, M., Bachmann, O., Fodor, L., Buret, Y., Dunkl, I., Sliwinski, J., Von Quadt, A., Peytcheva, I., Zimmerer, M., 2018. Early to Mid-Miocene syn-extensional massive silicic volcanism in the Pannonian Basin (East-Central Europe): Eruption chronology, correlation potential and geodynamic implications. Earth-Science Reviews, **179**: 1–19.

Lukács, R., Guillong, M., Bachmann, O., Fodor, L., Harangi, S., 2021. Tephrostratigraphy and magma evolution based on combined zircon trace element and U-Pb age data: Fingerprinting Miocene silicic pyroclastic rocks in the Pannonian Basin. Frontiers in Earth Science, **9**: 615768.

Martini, E., 1971. Standard Tertiary and Quaternary calcareous nannoplankton zonation. Proceedings of the 2nd Planktonic Conference, Roma, 1970, **2**: 739–785. Edizioni Tecnoscienza.

Mărunţeanu, M., 1999. Litho- and biostratigraphy (calcareous nannoplankton) of the Miocene deposits from the Outer Moldavides. Geologica Carpathica, **50**: 313–324.

Maţenco, L., Bertotti, G., 2000. Tertiary tectonic evolution of the external East Carpathians (Romania). Tectonophysics, **316**: 255–286.

McHargue, T., Pyrcz, M.J., Sullivan, M.D., Clark, J.D., Fildani, A., Romans, B.W., Covault, J.A., Levy, M., Posamentier, H.W., Drinkwater, N.J., 2011. Architecture of turbidite channel systems on the continental slope: patterns and predictions. Marine and Petroleum Geology, **28**: 728–743.

Medaris, G., Ducea, M., Ghent, E., Iancu, V., 2003. Conditions and timing of high-pressure Variscan metamorphism in the South Carpathians, Romania. Lithos, **70**: 141–161.

Melinte-Dobrinescu, M.C., Brustur, T., 2008. Oligocene–Lower Miocene events in Romania. Acta Palaeontologica Romaniae, **6**: 203–215.

Merten, S., Maţenco, L., Foeken, J.P.T., Stuart, F.M., Andriessen, P.A.M., 2010. From nappe stacking to out – of - sequence postcollisional deformations: Cretaceous to Quaternary exhumation history of the SE Carpathians assessed by low-temperature thermochronology. Tectonics, **29**: 1–28.

Moscardelli, L., Wood, L., 2008. New classification system for mass transport complexes in offshore Trinidad. Basin Research, **20**: 73–98.

Mrazec, L., Popescu-Voiteşti, I., 1914. Contributions à la connaissance des nappes du flysch carpathique en Roumanie (in French). Annuaire de l'Institut Geologique de Roumanie, **5**: 495–527.

Mulder, T., Alexander, J., 2001. The physical character of subaqueous sedimentary density currents and their deposits. Sedimentology, **48**: 269–299.

Murgeanu, G., Patrulius, D., Gherasi, N., Ghenea, A., Ghenea, C., 1968. Geological map of Romania: scale 1:200,000. Târgovişte sheet 35. Geological Institute of Romania, Bucharest.

Olteanu, F., 1952. Geological structure between Ursei and Câmpina region (in Romanian). Dări de Seamă ale Institutului Geologic, **36**: 125–139.

Owen, G., Moretti, M., 2011. Identifying triggers for liquefaction-induced soft-sediment deformation in sands. Sedimentary Geology, **235**: 141–147.

Pătruţ, I., 1955. Geology and tectonics of the Vălenii de Munte–Cosminele–Bustenari region (in Romanian). Anuarul Comitetului Geologic, **28**: 7–99.

Pearce, N.J.G., Westgate, J.A., Gualda, G.A.R., Gatti, E., Muhammad, R.F., 2020. Tephra glass chemistry provides storage and discharge details of five magma reservoirs which fed the 75 ka Youngest Toba Tuff eruption, northern Sumatra. Journal of Quaternary Science, **35**: 256–271.

Popescu, G., 1952. Paleogene flysch zone between Buzău Valley and Vărbilăului (short sum-up) (in Romanian). Dări de Seama ale Institutului Geologic, **36**: 113–125.

Posamentier, H.W., Walker, R.G., 2006. Deep water turbidites and submarine fans. SEPM Special Publication, **84**: 397–520.

Prentice, M., Pittari, A., Lowe, D.J., Kilgour, G., Kamp, P.J.J., Namaliu, M., 2022. Linking proximal ignimbrites and coeval distal tephra deposits to establish a record of voluminous Early Quaternary (2.4–1.9 Ma) volcanism of the Tauranga Volcanic Centre, New Zealand. Journal of Volcanology and Geothermal Research, **429**: 107595.

Răbăgia, T., Roban, R.D., Tărăpoancă, M., 2011. Sedimentary records of Paleogene (Eocene to Lowermost Miocene) deformations near the contact between the Carpathian thrust belt and Moesia. Oil & Gas Science and Technology, Revue d'IFP Energies Nouvelles, **66**: 931–952.

Raffi, I., Wade, B.S., Palike, H., Beu, A.G., Cooper, R., Crundwell, M.P., Krijgsman, W., Moore, T., Raine, I., Sardella, R., Vernyhorova, Y.V., 2020. The Neogene Period. In: Geologic Time Scale 2020 (eds. F.M. Gradstein, J.G. Ogg, M.D. Schmitz and G.M. Ogg): 1141–1215. Elsevier BV.

Roban, R.D., 2008. Sedimentological analysis of the Paleogene formations in the NE part of the Getic Depression: paleoenvironmental reconstructions (in Romanian). Ph.D. Thesis, Bucharest University, Romania.

Rocholl, A., Schaltegger, U., Gilg, H.A., Wijbrans, J., Bohme, M., 2018. The age of volcanic tuffs from the Upper Freshwater Molasse (North Alpine Foreland Basin) and their possible use for tephrostratigraphic correlations across Europe for the Middle Miocene. International Journal of Earth Sciences, **107**: 387–407.

Rubatto, D., Hermann, J., 2007. Experimental zircon/melt and zircon/garnet trace element partitioning and implications for the geochronology of crustal rocks. Chemical Geology, **241**: 38–61.

Rybár, S., Šarinová, K., Sant, K., Kuiper, K. F., Kováčová, M., Vojtko, R., Reiser, M. K., Fordinál, K., Teodoridis, V., Nováková, P., Vlček, V., 2019. New $^{40}Ar/^{39}Ar$, fission track and sedimentological data on a middle Miocene tuff occurring in the Vienna Basin: implications for the north-western Central Paratethys region. Geologica Carpathica, **70**: 386–404.

Sanders, C.A.E., Andriessen, P.A.M., Cloetingh, S.A.P.L., 1999. Life cycle of the East Carpathian orogen: Erosion history of a doubly vergent critical wedge assessed by fission-track thermochronology. Journal of Geophysical Research, **104**: 29095–29112.

Săndulescu, M., 1984. Romania's Geotectonics (in Romanian). Editura Tehnică, Bucharest.

Săndulescu, M., 1988. Cenozoic tectonic history of the Carpathians. AAPG Memoir, **45**: 17–25.

Săndulescu, M., Popescu, G., Mărunţeanu, M., 1995. Facies and stratigraphy of the Lower and Middle Miocene formations of the Slănic Syncline. Romanian Journal of Stratigraphy, **76**: 3–11.

Sant, K., Kuiper, K.F., Rybar, S., Grunert, P., Harzhauser, M., Mandic, O., Jamrich, M., Šarinová, K., Hudáčková, N., Krijgsman, W., 2020. $^{40}Ar/^{39}Ar$ geochronology using high sensitivity mass spectrometry: examples from middle Miocene horizons of the Central Paratethys. Geologica Carpathica, **71**: 166–182.

Šarinová, K., Rybár, S., Jourdan, F., Frew, A., Mayers, C., Kováčová, M., Lichtman, B., Nováková, P., Kováč, M., 2021. $^{40}Ar/^{39}Ar$ geochronology of Burdigalian palaeobotanical localities in the central Paratethys (south Slovakia). Geologica Acta, **19**: 1–19.

Sasvari, A., Baharev, A., 2014. SG2PS (structural geology to postscript converter) – a graphical solution for brittle structural data evaluation and paleostress calculation. Computers and Geosciences, **66**: 81–93.

Scharer, U., 1984. The effect of initial 230Th disequilibrium on young UPb ages: the Makalu case, Himalaya. Earth and Planetary Science Letters, **67**: 191–204.

Schleder, Z., Tămaş, D.M., Krézsek, C., Arnberger, K., Tulucan, A., 2019. Salt tectonics in the Bend Zone segment of the Carpathian fold and thrust belt, Romania. International Journal of Earth Sciences, **108**: 1595–1614.

Schmid, S.M., Bernoulli, D., Fugenschuh, B., Maţenco, L., Schefer, S., Schuster, R., Tischler, M., Ustaszewski, K., 2008. The Alpine–Carpathian–Dinaridic orogenic system: correlation and evolution of tectonic units. Swiss Journal of Geoscience, **101**: 139–183.

Sliwinski, J.T., Guillong, M., Liebske, C., Dunkl, I., Von Quadt, A., Bachmann, O., 2017. Improved accuracy of LA-ICP-MS U-Pb ages of Cenozoic zircons by alpha dose correction. Chemical Geology, **472**: 8–21.

Sprague, A.R.G., Garfield, T.R., Goulding, F.J., Beaubouef, R.T., Sullivan, M.D., Rossen, C., Campion, K.M., Sickafoose, D.K., Abreu, V., Schellpeper, M.E., Jensen, G.N., Jennette, D.C., Pirmez, C., Dixon, B.T., Ying, D., Ardill, J., Mohrig, D.C., Porter, M.L., Farrel, M.E., Mellere, D., 2005. Integrated slope channel depositional models: the key to successful prediction of reservoir presence and quality in offshore West Africa. CIPM Cuarto E-Exitep, 1–13.

Ştefănescu, M., 1995. Stratigraphy and structure of the Cretaceous and Paleogene flysch deposits between Prahova and Ialomiţa valleys. Romanian Journal of Tectonics and Regional Geology, **76**: 1–49.

Ştefănescu, M., Mărunţeanu, M., 1980. Age of the Doftana Mollase. Dări de Seamă ale Institutului de Geologie şi Geofizică, **65**: 169–182.

Ştefănescu, M., Ghenea, C., Papaianopol, I., Ghenea, A., Mihăilescu, N., Ivan, T., Munteanu, T., Ştefănescu, M., Munteanu, E., 1988. Geological map of Romania: scale 1:50,000. Pucioasa Sheet. Geological Institute of Romania, Bucharest.

Ştefănescu, M., Popescu, I., Ivan, V., Melinte, M., 1993. Aspect of the possibilities of lithological correlation of Oligocene-Lower Miocene deposits of the Buzau Valley. Romanian Journal of Stratigraphy, **75**: 89–90.

Sylvester, Z., Lowe, D.R., 2004. Textural trends in turbidites and slurry beds from Oligocene flysch of the Eastern Carpathians, Romania. Sedimentology, **51**: 945–972.

Szabo, B., 2012. Reconstruction of the Paleogene and Neogene marine paleoenvironments in the southernmost part of the Tarcău Nappe (East Carpathians) based on fossil foraminifera assemblages. Ph.D. Thesis, Babeş-Bolyai University, Cluj-Napoca, Romania.

Szabo, B., Bercea, R., Iordache, G., Székely, S.F., Petruţa, S., Filipescu, S., Săsăran, E., Bălc, R., 2010. New data on the sedimentary facies and micropaleontology from Pucioasa (Dâmboviţa District). In: 1st International Geosciences Student Conference (eds. A. Rîcu et al.), Bucharest, Abstracts book: 149.

Szakács, A., Pécskay, Z., Silye, L., Balogh, K., Vlad, D., Fülop, A., 2012. On the age of the Dej Tuff, Transylvanian Basin (Romania). Geologica Carpathica, **63**: 139–148.

Talling, P.J., Masson, D.G., Sumner, E.J., Malgesini, G., 2012. Subaqueous sediment density flows: Depositional processes and deposit types. Sedimentology, **59**: 1937–2003.

Tămaş, D.M., 2018. Salt tectonics in the Eastern Carpathian Bend Zone, Romania. Ph.D. Thesis, Babeş-Bolyai University, Cluj-Napoca, Romania.

Tămaş, A., Tămaş, D.M., Krézsek, C., Schleder, Z., Palladino, G., Bercea, R., 2020. The nature and significance of sand intrusions in a hydrocarbon-rich fold and thrust belt: eastern Carpathians Bend Zone, Romania. Journal of the Geological Society, **177**: 343–356.

Tinterri, R., Magalhaes, P.M., Tagliafferi, A., Cunha, R.S., 2016. Convolute laminations and load structures in turbidites as indicators of flow reflections and decelerations against bounding slopes. Examples from the Marnoso-Arenacea Formation (northern Italy) and Annot Sandstones (south eastern France). Sedimentary Geology, **344**: 382–407.

Ustaszewski, K., Schmid, S.M., Fügenschuh, B., Tischler, M., Kissling, E., Spakman, W., 2008. A map-view restoration of the Alpine-Carpathian-Dinaridic system for the Early Miocene. Swiss Journal of Geosciences, **101**: 273–294.

Wade, B., Pearson, P.N., Berggren, W.A., Palike, H., 2011. Review and revision of Cenozoic tropical planktonic foraminiferal biostratigraphy and calibration to the geomagnetic polarity and astronomical time scale. Earth-Science Reviews, **104**: 111–142.

Young, J.R., Bown, P.R., Lees, J.A., 2017. Nannotax3 website. International Nannoplankton Association. URL: http://www.mokrotaz.org/Nannotax3

Zavala, C., Arcuri, M., 2016. Intrabasinal and Extrabasinal turbidites: origin and distinctive characteristics. Sedimentary Geology, **337**: 36–54.

APPENDIX 1

Zircon U-Pb age dating analyses: summary of reference material analyses and sample data

1 – weighted mean average; 2 – propagated 2SE without Ssys; 3 – MSWD; 4 – no. analyses; 5 – average rel. 2SE of individual analyses

Session	GJ-1[1]					Plesovice[2]					91500[3]					AUSZ7-1[4]					AUSZ7-5[5]				
	Ref. age: 601.9 Ma					Ref. age: 337.15 Ma					Ref. age: 1063.5 Ma					Ref. age: 38.89 Ma					Ref. age: 2.409 Ma				
	1	2	3	4	5	1	2	3	4	5	1	2	3	4	5	1	2	3	4	5	1	2	3	4	5
2021118_1b																									
uncorrected	602	1.1	0.8	39	1.19	339.1	1.6	1.2	10	1.23	1056.6	3.6	0.94	11	1.17	38.29	0.26	0.83	10	2.3	2.365	0.081	1.5	11	8.6
shift corrected	601.6	1.1	0.83	39	1.17	337.9	1.2	0.95	10	1.23	1063	3.6	0.84	11	1.17	38.63	0.25	0.89	10	2.3	2.377	0.08	1.5	11	8.5
Th disequilibrium corrected																38.7	0.25	0.89	10	2.3	2.45	0.08	1.5	11	8.2

[1] – Jackson et al. (2004); Horstwood et al. (2016)

[2] – Sláma et al. (2008); Horstwood et al. (2016)

[3] – Wiedenbeck et al. (1995); Horstwood et al. (2016)

[4] – Kennedy et al. (2014); ID-TIMS dating of University of Geneva: 38.896 ±0.05 Ma

[5] – von Quadt et al. (2016); ID-TIMS dating of ETH, Zürich: 2.4095 ±0.0017 Ma

References

Horstwood, M.S.A., Kosler, J., Gehrels, G., Jackson, S.E., Mclean, N.M., Paton, C., Pearson, N.J., Sircombe, K., Sylvester, P., Vermeesch, P., Bowring, J.F., Condon, D.J., Schoene, B., 2016. Community-derived standards for La-Icp-Ms U-(Th-)Pb geochronology –uncertainty propagation, age interpretation and data reporting. Geostandards and Geoanalytical Research, **40**: 311–332.

Jackson, S.E., Pearson, N.J., Griffin, W.L., Belousova, E.A., 2004. The application of laser ablation-inductively coupled plasma-mass spectrometry to in situ U-Pb zircon geochronology. Chemical Geology, **211**: 47–69.

Kennedy, A.K., Wotzlaw, J.-F., Schaltegger, U., Crowley, J.L., Schmitz, M., 2014. Eocene zircon reference material for microanalysis of U-Th-Pb isotopes and trace elements. The Canadian Mineralogist, **52**: 409–421.

Slama, J., Kosler, J., Condon, D.J., Crowley, J.L., Gerdes, A., Hanchar, J.M., Horstwood, M.S.A., Morris, G.A., Nasdala, L., Norberg, N., Schaltegger, U., Schoene, B., Tubrett, M.N., Whitehouse, M.J., 2008. Plešovice zircon – a new natural reference material for U-Pb and Hf isotopic microanalysis. Chemical Geology, **249**: 1–35.

von Quadt, A., Wotzlaw, J.-F., Buret, Y., Large, S.J.E., Peytcheva, I., Trinquier, A., 2016. High-precision zircon U/Pb geochronology by ID-TIMS using new 1013 ohm resistors. Journal of Analytical Atomic Spectrometry, **31**: 658–665.

Wiedenbeck, M., Alle, P., Corfu, F., Griffin, W.L., Meier, M., Oberli, F., Quadt, O.V., Roddick, J.C., Spiegel, W., 1995. Three natural zircon standards for U-Th-Pb, Lu-Hf, trace element and REE Analyses. Geostandards Newsletter, **19**: 1–23.

			Isotopic ratios							
Sample	Position	Duration (s)	Final207_235	Final207_235_Prop 2SE	Final206_238	Final206_238_ Prop2SE	Final207_206	Final207_206_ Prop2SE	Final208_232	Final208_232 _Prop2SE
LR__42_RB_1 - 1	rim	26.857	0.595	0.049	0.00776	0.00047	0.538	0.019	0.0184	0.0014
LR__42_RB_1 - 2	rim	25.891	0.0171	0.00077	0.002631	0.000038	0.0469	0.002	0.000789	0.000046
LR__42_RB_1 - 3	rim	22.027	0.0181	0.00086	0.002644	0.000042	0.0497	0.0026	0.000833	0.000051
LR__42_RB_1 - 4	rim of 5	17.389	0.01729	0.00071	0.002644	0.000062	0.047	0.002	0.000857	0.000054
LR__42_RB_1 - 5	interior of 4	16.037	0.01775	0.0011	0.002715	0.000044	0.0472	0.003	0.000831	0.00005
LR__42_RB_1 - 6	rim	15.844	0.01696	0.0012	0.00268	0.000045	0.0466	0.0029	0.000837	0.000074
LR__42_RB_1 - 7	rim	23.959	0.01823	0.00089	0.002733	0.000056	0.0483	0.0021	0.000933	0.000074
LR__42_RB_1 - 8	rim of 9	18.549	0.01741	0.0009	0.00265	0.000048	0.0477	0.002	0.000815	0.000058
LR__42_RB_1 - 9	interior of 8	16.23	0.0222	0.0059	0.00271	0.000098	0.0583	0.012	0.00095	0.00018
LR__42_RB_1 - 10	interior	14.684	0.0529	0.0025	0.00773	0.00033	0.0502	0.0014	0.002032	0.00015
LR__42_RB_1 - 11	rim	13.139	0.0187	0.00095	0.002734	0.000046	0.0507	0.0021	0.000788	0.000056
LR__42_RB_1 - 12	rim	23.379	0.01669	0.00097	0.002648	0.000047	0.0461	0.0028	0.000857	0.000053
LR__42_RB_1 - 13	rim	26.857	0.1523	0.0066	0.01916	0.00088	0.0573	0.0022	0.00859	0.00052
LR__42_RB_1 - 14	rim	16.23	0.01781	0.0006	0.002687	0.000042	0.0481	0.0015	0.000798	0.000047
LR__42_RB_1 - 15	rim	26.084	0.01747	0.00067	0.002626	0.000039	0.0483	0.0019	0.000799	0.000057
LR__42_RB_1 - 16	rim of 17	22.799	0.01827	0.00094	0.002728	0.00014	0.0482	0.0017	0.000854	0.000093
LR__42_RB_1 - 17	rim of 16	26.857	0.02044	0.00062	0.002669	0.00004	0.0547	0.0016	0.000911	0.000046
LR__42_RB_1 - 18	rim	22.413	0.01796	0.00087	0.002725	0.000049	0.0477	0.0021	0.000849	0.000057
LR__42_RB_1 - 19	rim	20.288	0.01676	0.00079	0.002653	0.000046	0.0455	0.0017	0.000815	0.000047
LR__42_RB_1 - 20	rim	20.094	0.0192	0.0014	0.00281	0.000047	0.0494	0.0027	0.000912	0.000065
LR__42_RB_1 - 21	rim	26.897	0.0231	0.0011	0.002707	0.000041	0.0619	0.0028	0.000962	0.000057
LR__42_RB_1 - 22	rim	20.674	0.0183	0.0012	0.002749	0.000047	0.048	0.0029	0.000908	0.000064
LR__42_RB_1 - 23	rim	22.799	0.01857	0.001	0.002772	0.000039	0.0489	0.0023	0.000829	0.000055
LR__42_RB_1 - 24	rim	22.22	0.01849	0.001	0.00285	0.000064	0.0474	0.0022	0.000863	0.000068
LR__42_RB_1 - 25	rim	16.81	0.01763	0.00091	0.002658	0.000064	0.0473	0.0019	0.000816	0.000072
LR__42_RB_1 - 26	rim	11.013	0.01775	0.00086	0.002653	0.000044	0.0493	0.0021	0.000874	0.00006
LR__42_RB_1 - 27	rim	14.878	0.0184	0.0012	0.002728	0.000058	0.0486	0.0028	0.000816	0.00008
LR__42_RB_1 - 28	rim	23.186	0.01833	0.00074	0.002739	0.000047	0.0486	0.0017	0.000793	0.000053
LR__42_RB_1 - 29	rim	10.24	0.0181	0.0028	0.00265	0.000059	0.0489	0.0068	0.000808	0.0001
LR__42_RB_1 - 30	rim	26.896	0.0274	0.0017	0.002744	0.000045	0.0725	0.0039	0.001051	0.000066
LR__42_RB_1 - 31	rim	17.196	0.0166	0.00091	0.002627	0.000052	0.0458	0.0026	0.000757	0.000051
LR__42_RB_1 - 32	rim	24.345	0.01701	0.00087	0.002616	0.000044	0.0469	0.0022	0.000816	0.000056
LR__42_RB_1 - 33	rim	22.606	0.01734	0.00092	0.002693	0.000044	0.0466	0.0022	0.000835	0.000058
LR__42_RB_1 - 34	rim	26.908	0.066	0.015	0.00314	0.00014	0.146	0.029	0.00211	0.00043
LR__42_RB_1 - 35	interior	22.606	0.0183	0.0012	0.002814	0.00006	0.0473	0.0032	0.000947	0.000081
LR__42_RB_1 - 36	rim	23.186	0.01813	0.00074	0.002651	0.000036	0.0496	0.0018	0.000806	0.000045
LR__42_RB_1 - 37	rim	23.766	0.0175	0.001	0.00272	0.000052	0.0463	0.003	0.0009	0.000077
LR__42_RB_1 - 38	rim	26.879	0.0329	0.0024	0.002855	0.000044	0.0814	0.0056	0.001381	0.0001
LR__42_RB_1 - 39	rim	13.912	0.2107	0.0058	0.02988	0.00069	0.05146	0.00082	0.00899	0.00048
LR__42_RB_1 - 40	rim	24.732	0.017	0.00063	0.00262	0.000042	0.047	0.0021	0.000796	0.000052
LR__42_RB_1 - 41	rim	20.674	0.01706	0.00076	0.002737	0.000043	0.0459	0.0018	0.000839	0.000052
LR__42_RB_1 - 42	rim	10.434	0.018	0.054	0.002736	0.00047	0.049	0.058	0.000839	0.0016
LR__42_RB_1 - 43	rim of 44	16.617	0.01859	0.00066	0.002699	0.000042	0.0492	0.0017	0.000803	0.00005

			Isotopic ratios							
Sample	Position	Duration (s)	Final207_235	Final207_235_Prop 2SE	Final206_238	Final206_238_ Prop2SE	Final207_206	Final207_206_ Prop2SE	Final208_232	Final208_232 _Prop2SE
LR__42_RB_1 - 44	rim of 43	23.379	0.0182	0.00098	0.002713	0.000044	0.0494	0.0026	0.000817	0.000052
LR__42_RB_1 - 45	rim	22.606	0.01754	0.00089	0.002737	0.000045	0.0467	0.0022	0.000765	0.00006
LR__42_RB_1 - 46	rim	26.896	0.0273	0.0027	0.002738	0.000058	0.0689	0.0051	0.00121	0.00012
LR__42_RB_1 - 47	rim	26.916	0.0174	0.00066	0.002672	0.000037	0.0471	0.0016	0.000811	0.00005
LR__42_RB_1 - 48	rim	18.935	0.01867	0.00062	0.002685	0.000037	0.0494	0.0017	0.000819	0.000047
LR__42_RB_1 - 49	rim	22.413	0.01752	0.0006	0.002686	0.000034	0.0471	0.0015	0.000822	0.000045
LR__42_RB_1 - 50	rim	25.118	0.2681	0.0061	0.03803	0.0005	0.05138	0.00087	0.0119	0.00063
LR__42_RB_1 - 51	rim	21.06	0.0181	0.0013	0.002731	0.000057	0.0478	0.0035	0.000813	0.00008
LR__42_RB_1 - 52	rim	20.674	0.0184	0.001	0.002713	0.000053	0.0491	0.0029	0.000867	0.000068
LR__42_RB_1 - 53	rim	26.664	0.01843	0.00068	0.002768	0.00004	0.0481	0.0019	0.000841	0.000049
LR__42_RB_1 - 54	rim	16.423	0.0191	0.00086	0.002738	0.000046	0.0488	0.0021	0.000902	0.000058
LR__42_RB_1 - 55	rim	22.027	0.01795	0.00073	0.002703	0.000039	0.0481	0.0019	0.00083	0.000054
LR__42_RB_1 - 56	rim	14.298	0.0184	0.0031	0.00272	0.000068	0.0495	0.0077	0.000858	0.000071
LR__42_RB_1 - 57	rim	19.515	0.0178	0.00094	0.002685	0.000045	0.0489	0.0024	0.000845	0.000055
LR__42_RB_1 - 58	rim of 59	18.355	0.01797	0.00083	0.002732	0.00004	0.0477	0.0021	0.000836	0.000057
LR__42_RB_1 - 59	rim of 58	23.379	0.01708	0.00066	0.002649	0.000041	0.0461	0.0017	0.000866	0.000057
LR__42_RB_1 - 60	core of 58	12.752	0.0204	0.0016	0.002832	0.000063	0.0518	0.0038	0.00079	0.00009
LR__42_RB_1 - 61	rim	18.162	0.01681	0.00068	0.002645	0.000047	0.0459	0.0019	0.000855	0.000055
LR__42_RB_1 - 62	interior	18.162	0.017	0.00086	0.002654	0.000059	0.0455	0.002	0.000814	0.00005
LR__42_RB_1 - 63	rim	21.833	0.01718	0.00078	0.002735	0.00005	0.0448	0.0022	0.000865	0.000071
LR__42_RB_1 - 64	rim	28.789	0.01713	0.00079	0.002611	0.000041	0.0473	0.0019	0.000779	0.000051
LR__42_RB_1 - 65	rim	10.24	0.0182	0.0018	0.002659	0.000057	0.0498	0.0037	0.000857	0.000083
LR__42_RB_1 - 66	rim	21.06	0.0196	0.0011	0.0028	0.000044	0.0502	0.0025	0.000882	0.000074
LR__42_RB_1 - 67	rim	18.549	0.0183	0.0016	0.002764	0.000057	0.0494	0.0035	0.000848	0.000075
LR__42_RB_1 - 68	rim	16.423	0.0177	0.00076	0.002696	0.000039	0.0475	0.0018	0.000797	0.000053
LR__42_RB_1 - 69	rim	16.617	0.018	0.00099	0.002643	0.000044	0.049	0.0026	0.000812	0.000056
LR__42_RB_1 - 70	rim	23.186	0.017	0.00094	0.002723	0.000047	0.0455	0.0026	0.000804	0.000059
LR__42_RB_1 - 71	rim	24.345	0.01758	0.00071	0.002647	0.000052	0.048	0.0018	0.000759	0.000062

Abbreviations

Int – internal
Prop – propagated
Approx – approximate
CPS – counts per second
SE – standard error
s – second
logDose – logarithm of the alpha radiation dose, calculated as given in equations (1) in Sliwinski et al. (2017)

Reference

Sliwinski, J.T., Guillong, M., Liebske, C., Dunkl, I., Quadt, A.V., Bachmann, O, 2017. Improved accuracy of LA-ICP-MS U-Pb ages of Cenozoic zircons by alpha dose correction. Chemical Geology, **472:** 8–21.

	Calculated dates							
Sample	FinalAge207_235	FinalAge207_235_Prop2SE	FinalAge206_238	FinalAge206_238_Prop2SE	FinalAge208_232	FinalAge208_232_Prop2SE	FinalAge207_206	FinalAge207_206_Prop2SE
LR__42_RB_1 - 1	480	32	49.8	3	368	27	4340	55
LR__42_RB_1 - 2	17.21	0.77	16.94	0.24	15.94	0.94	57	83
LR__42_RB_1 - 3	18.21	0.85	17.02	0.27	16.82	1	180	110
LR__42_RB_1 - 4	17.41	0.71	17.02	0.4	17.31	1.1	62	85
LR__42_RB_1 - 5	17.86	1.1	17.48	0.28	16.79	1	70	120
LR__42_RB_1 - 6	17.07	1.2	17.25	0.29	16.9	1.5	70	120
LR__42_RB_1 - 7	18.34	0.89	17.6	0.36	18.9	1.5	115	95
LR__42_RB_1 - 8	17.52	0.89	17.06	0.31	16.46	1.2	115	87
LR__42_RB_1 - 9	22.2	5.7	17.45	0.63	19.2	3.7	560	320
LR__42_RB_1 - 10	52.3	2.6	49.67	2.1	41	3.1	217	61
LR__42_RB_1 - 11	18.8	0.94	17.6	0.29	15.92	1.1	220	90
LR__42_RB_1 - 12	16.81	0.97	17.05	0.3	17.31	1.1	10	110
LR__42_RB_1 - 13	143.8	5.8	122.3	5.6	174.6	11	509	83
LR__42_RB_1 - 14	17.93	0.59	17.3	0.27	16.12	0.95	105	66
LR__42_RB_1 - 15	17.59	0.67	16.91	0.25	16.15	1.2	128	86
LR__42_RB_1 - 16	18.38	0.94	17.56	0.88	17.3	1.9	110	72
LR__42_RB_1 - 17	20.55	0.62	17.18	0.26	18.4	0.92	391	65
LR__42_RB_1 - 18	18.07	0.87	17.55	0.32	17.15	1.1	95	90
LR__42_RB_1 - 19	16.87	0.79	17.08	0.29	16.46	0.94	-2	76
LR__42_RB_1 - 20	19.3	1.3	18.09	0.3	18.4	1.3	150	100
LR__42_RB_1 - 21	23.2	1.1	17.42	0.27	19.43	1.2	692	95
LR__42_RB_1 - 22	18.4	1.2	17.7	0.3	18.3	1.3	110	110
LR__42_RB_1 - 23	18.68	1	17.85	0.25	16.76	1.1	141	96
LR__42_RB_1 - 24	18.6	1	18.34	0.41	17.4	1.4	79	91
LR__42_RB_1 - 25	17.75	0.91	17.11	0.41	16.5	1.5	71	83
LR__42_RB_1 - 26	17.86	0.86	17.08	0.28	17.7	1.2	160	89
LR__42_RB_1 - 27	18.5	1.2	17.56	0.37	16.5	1.6	130	120
LR__42_RB_1 - 28	18.45	0.73	17.63	0.3	16.02	1.1	129	78
LR__42_RB_1 - 29	18.2	2.8	17.06	0.38	16.3	2.1	140	220
LR__42_RB_1 - 30	27.5	1.7	17.66	0.29	21.23	1.3	1000	120
LR__42_RB_1 - 31	16.7	0.91	16.91	0.34	15.3	1	20	110
LR__42_RB_1 - 32	17.28	0.87	16.84	0.28	16.48	1.1	80	99
LR__42_RB_1 - 33	17.45	0.91	17.34	0.28	16.87	1.2	43	98
LR__42_RB_1 - 34	64	14	20.24	0.9	42.6	8.7	1810	450
LR__42_RB_1 - 35	18.5	1.2	18.11	0.38	19.1	1.6	80	140
LR__42_RB_1 - 36	18.24	0.74	17.07	0.23	16.28	0.91	154	81
LR__42_RB_1 - 37	17.6	1	17.51	0.34	18.2	1.6	40	120
LR__42_RB_1 - 38	32.8	2.4	18.38	0.28	27.9	2	1180	130
LR__42_RB_1 - 39	194.1	4.9	189.8	4.3	180.9	9.7	259	39
LR__42_RB_1 - 40	17.11	0.63	16.87	0.27	16.08	1	61	90
LR__42_RB_1 - 41	17.18	0.76	17.62	0.28	16.95	1.1	12	81
LR__42_RB_1 - 42	18.1	46	17.61	3	17	33	150	580
LR__42_RB_1 - 43	18.7	0.66	17.38	0.27	16.22	1	152	75

	Calculated dates							
Sample	FinalAge207_235	FinalAge207_235_Prop2SE	FinalAge206_238	FinalAge206_238_Prop2SE	FinalAge208_232	FinalAge208_232_Prop2SE	FinalAge207_206	FinalAge207_206_Prop2SE
LR__42_RB_1 - 44	18.3	0.98	17.47	0.28	16.5	1.1	160	110
LR__42_RB_1 - 45	17.65	0.89	17.62	0.29	15.46	1.2	48	92
LR__42_RB_1 - 46	27.3	2.6	17.62	0.37	24.5	2.3	870	160
LR__42_RB_1 - 47	17.51	0.66	17.2	0.24	16.39	1	64	71
LR__42_RB_1 - 48	18.78	0.61	17.29	0.24	16.55	0.94	181	73
LR__42_RB_1 - 49	17.64	0.6	17.29	0.22	16.62	0.91	61	64
LR__42_RB_1 - 50	241.1	4.8	240.6	3.1	239	12	256	40
LR__42_RB_1 - 51	18.2	1.3	17.58	0.37	16.4	1.6	100	150
LR__42_RB_1 - 52	18.5	1	17.46	0.34	17.5	1.4	150	120
LR__42_RB_1 - 53	18.54	0.67	17.82	0.26	16.98	0.99	121	81
LR__42_RB_1 - 54	19.2	0.85	17.63	0.29	18.2	1.2	170	91
LR__42_RB_1 - 55	18.06	0.73	17.4	0.25	16.76	1.1	110	80
LR__42_RB_1 - 56	18.5	3	17.51	0.44	17.3	1.4	160	230
LR__42_RB_1 - 57	17.91	0.93	17.29	0.29	17.07	1.1	160	100
LR__42_RB_1 - 58	18.09	0.82	17.59	0.26	16.9	1.2	90	88
LR__42_RB_1 - 59	17.19	0.66	17.05	0.26	17.49	1.2	19	75
LR__42_RB_1 - 60	20.5	1.6	18.23	0.4	16	1.8	260	150
LR__42_RB_1 - 61	16.93	0.68	17.03	0.3	17.3	1.1	18	80
LR__42_RB_1 - 62	17.1	0.86	17.09	0.38	16.44	1	0	83
LR__42_RB_1 - 63	17.29	0.78	17.61	0.32	17.5	1.4	-32	91
LR__42_RB_1 - 64	17.24	0.79	16.81	0.26	15.74	1	77	80
LR__42_RB_1 - 65	18.3	1.8	17.12	0.37	17.3	1.7	180	140
LR__42_RB_1 - 66	19.7	1.1	18.02	0.28	17.8	1.5	190	99
LR__42_RB_1 - 67	18.4	1.6	17.8	0.37	17.14	1.5	160	140
LR__42_RB_1 - 68	17.82	0.76	17.35	0.25	16.1	1.1	82	83
LR__42_RB_1 - 69	18.1	0.98	17.01	0.28	16.4	1.1	150	110
LR__42_RB_1 - 70	17.11	0.94	17.53	0.3	16.24	1.2	0	110
LR__42_RB_1 - 71	17.69	0.71	17.04	0.33	15.33	1.2	105	78

	Corrected dates														
Sample	Corrected Age*	CorrectedAge_2SE	Th_corrected_Age	Th_corrected_Age_2SE	logDose	Approx_U_PPM	Approx_Th_PPM	Pb206_CPS	Pb206_CPS_Int2SE	Pb207_CPS	Pb207_CPS_Int2SE	U238_CPS	U238_CPS_Int2SE	Discordance	Th/U
LR__42_RB_1 - 1	52.414	3.3798	52.486	3.37979	17.1211	703	469	1.19E+05	8.10E+03	6.26E+04	6.30E+03	1.63E+07	3.00E+05	89.63	0.68
LR__42_RB_1 - 2	17.138	0.253646	17.211	0.254015	16.9124	1217	1128	70160	670	3260	110	2.81E+07	4.00E+05	1.57	0.93
LR__42_RB_1 - 3	17.22	0.278168	17.293	0.278503	16.698	760	598	44320	930	2180	110	1.76E+07	4.40E+05	6.53	0.77
LR__42_RB_1 - 4	17.348	0.419724	17.421	0.419943	16.8955	1215	870	6.89E+04	1.30E+03	3226	95	2.81E+07	4.30E+05	2.24	0.72
LR__42_RB_1 - 5	17.7	0.293198	17.773	0.293516	16.8042	945	743.8	53840	820	2520	110	2.19E+07	3.20E+05	2.13	0.80
LR__42_RB_1 - 6	17.425	0.29397	17.498	0.294286	16.4488	446.6	230.6	26300	730	1188	75	1.03E+07	1.50E+05	-1.05	0.52
LR__42_RB_1 - 7	17.826	0.369335	17.898	0.369585	16.5294	529	263.9	3.19E+04	1.20E+03	1538	92	1.22E+07	5.80E+05	4.03	0.50
LR__42_RB_1 - 8	17.285	0.318626	17.358	0.318918	16.6812	766	420	4.50E+04	2.40E+03	2120	130	1.77E+07	1.10E+06	2.63	0.56
LR__42_RB_1 - 9	17.602	0.628549	17.675	0.628691	15.7534	84.7	64.2	4980	200	287	50	1.96E+06	7.00E+04	21.40	0.77
LR__42_RB_1 - 10	51.197	2.26634	51.27	2.26636	17.3327	1102	958	1.93E+05	4.80E+03	9570	480	2.55E+07	3.80E+05	5.03	0.88
LR__42_RB_1 - 11	17.805	0.303572	17.878	0.303879	16.6166	593	548.3	36330	780	1780	130	1.37E+07	3.40E+05	6.38	0.94
LR__42_RB_1 - 12	17.268	0.311884	17.341	0.312183	16.6844	722	635	4.24E+04	3.80E+03	1900	220	1.67E+07	1.40E+06	-1.43	0.79
LR__42_RB_1 - 13	127.106	6.1051	127.178	6.10505	17.0125	232.3	102.3	9.49E+04	5.00E+03	5380	280	5.38E+06	1.30E+05	14.95	0.45
LR__42_RB_1 - 14	17.522	0.281215	17.595	0.281547	16.9542	1265	1415	7.21E+04	1.60E+03	3380	140	2.93E+07	3.20E+05	3.51	1.13
LR__42_RB_1 - 15	17.096	0.258627	17.169	0.258988	16.7486	914	447	5.19E+04	1.80E+03	2440	130	2.12E+07	9.30E+05	3.87	0.49
LR__42_RB_1 - 16	18.23	0.975381	18.303	0.975466	16.6773	743	381	4.32E+04	1.30E+03	2050	100	1.72E+07	8.30E+05	4.46	0.52
LR__42_RB_1 - 17	17.396	0.267855	17.469	0.268204	17.1028	1915	1494	1.13E+05	1.90E+03	6150	200	4.43E+07	1.20E+06	16.40	0.79
LR__42_RB_1 - 18	17.785	0.32678	17.858	0.327065	16.7667	895	546	5.31E+04	1.20E+03	2460	120	2.07E+07	2.80E+05	2.88	0.61
LR__42_RB_1 - 19	17.324	0.308743	17.397	0.309045	16.938	1316	1036	76650	720	3480	150	3.05E+07	5.20E+05	-1.24	0.79
LR__42_RB_1 - 20	18.28	0.308176	18.353	0.308478	16.5143	479	324	2.89E+04	1.40E+03	1410	120	1.11E+07	7.50E+05	6.27	0.67
LR__42_RB_1 - 21	17.614	0.270571	17.687	0.270916	16.6554	692	450	4.09E+04	2.00E+03	2500	170	1.60E+07	9.90E+05	24.91	0.66
LR__42_RB_1 - 22	17.92	0.311984	17.993	0.312282	16.7078	800	367	4.87E+04	4.80E+03	2290	240	1.85E+07	2.00E+06	3.80	0.46
LR__42_RB_1 - 23	18.024	0.257037	18.097	0.2574	16.6605	658	551	39640	940	1920	120	1.52E+07	5.50E+05	4.44	0.85
LR__42_RB_1 - 24	18.596	0.421326	18.668	0.421545	16.4662	435	235	2.72E+04	1.70E+03	1280	100	1.01E+07	7.40E+05	1.40	0.55
LR__42_RB_1 - 25	17.4	0.426949	17.473	0.427165	16.6265	629	556	3.73E+04	3.10E+03	1690	160	1.45E+07	1.30E+06	3.61	0.87
LR__42_RB_1 - 26	17.29	0.292052	17.363	0.292371	16.7183	832	463	45020	660	2200	100	1.92E+07	5.10E+05	4.37	0.56
LR__42_RB_1 - 27	17.77	0.379372	17.843	0.379616	16.3851	376	207.8	23020	630	1082	97	8.70E+06	3.00E+05	5.08	0.55
LR__42_RB_1 - 28	17.852	0.311557	17.925	0.311855	16.6827	707	563	4.20E+04	1.50E+03	2003	76	1.63E+07	8.30E+05	4.44	0.80
LR__42_RB_1 - 29	17.343	0.394821	17.416	0.395055	16.7132	786	615	4.37E+04	1.40E+03	2120	250	1.82E+07	5.40E+05	6.26	0.79
LR__42_RB_1 - 30	17.878	0.298279	17.951	0.298591	16.7007	732	601	4.38E+04	2.60E+03	3040	160	1.69E+07	1.20E+06	35.78	0.83
LR__42_RB_1 - 31	17.147	0.344982	17.22	0.345251	16.633	633.9	623	34830	850	1560	100	1.46E+07	2.00E+05	-1.26	0.98
LR__42_RB_1 - 32	17.04	0.290729	17.113	0.29105	16.6349	678	465	3.89E+04	3.40E+03	1840	160	1.56E+07	1.10E+06	2.55	0.66
LR__42_RB_1 - 33	17.525	0.289422	17.598	0.289744	16.5729	555	458	31840	980	1447	75	1.28E+07	6.60E+05	0.63	0.83
LR__42_RB_1 - 34	20.756	0.94546	20.829	0.945549	16.4533	360	302	2.39E+04	1.10E+03	3030	560	8.30E+06	6.80E+05	68.38	0.83
LR__42_RB_1 - 35	18.325	0.391994	18.398	0.392229	16.3662	348	197.3	21560	770	1017	83	8.02E+06	3.20E+05	2.11	0.56
LR__42_RB_1 - 36	17.254	0.239679	17.327	0.240069	16.8792	1150	905.7	67020	750	3270	120	2.65E+07	4.70E+05	6.41	0.78
LR__42_RB_1 - 37	17.704	0.340089	17.777	0.340362	16.423	409.5	235.8	24020	350	1089	70	9.44E+06	1.50E+05	0.51	0.57
LR__42_RB_1 - 38	18.586	0.291118	18.659	0.291438	16.696	729	431	4.55E+04	2.10E+03	3700	400	1.68E+07	9.30E+05	43.96	0.58
LR__42_RB_1 - 39	188.796	4.22339	188.867	4.22336	17.9056	1069	914	7.18E+05	9.30E+03	36340	710	2.47E+07	7.50E+05	2.22	0.85
LR__42_RB_1 - 40	17.076	0.27941	17.149	0.279744	16.775	950	575	54310	900	2456	88	2.19E+07	7.00E+05	1.40	0.60
LR__42_RB_1 - 41	17.827	0.285173	17.9	0.285499	16.728	785	626.1	46270	910	2042	91	1.81E+07	5.90E+05	-2.56	0.80
LR__42_RB_1 - 42	19.927	3.87788	20	3.87786	16.6043	605	411	3.38E+04	1.70E+03	1620	100	1.39E+07	8.90E+05	2.71	0.68
LR__42_RB_1 - 43	17.579	0.278702	17.652	0.279036	16.742	828	629.8	50100	820	2421	95	1.91E+07	4.10E+05	7.06	0.76

	Corrected dates														
Sample	Corrected Age*	CorrectedAge_ 2SE	Th_corrected _Age	Th_corrected_ Age_2SE	logDose	Approx_ U_PPM	Approx_ Th_PPM	Pb206_CPS	Pb206_CPS _Int2SE	Pb207_CPS	Pb207_CPS_ Int2SE	U238_CPS	U238_CPS _Int2SE	Discordance	Th/U
LR__42_RB_1 - 44	17.662	0.290239	17.735	0.29056	16.6224	652	364	3.86E+04	1.10E+03	1830	110	1.50E+07	5.30E+05	4.54	0.54
LR__42_RB_1 - 45	17.834	0.298402	17.906	0.298714	16.7067	783	445.7	46650	700	2136	90	1.80E+07	3.90E+05	0.17	0.57
LR__42_RB_1 - 46	17.82	0.377903	17.893	0.378148	16.3218	324.8	175.2	19520	660	1240	120	7.48E+06	1.70E+05	35.46	0.54
LR__42_RB_1 - 47	17.393	0.246363	17.466	0.246742	16.8712	1166	690	6.83E+04	1.70E+03	3180	130	2.68E+07	8.60E+05	1.77	0.59
LR__42_RB_1 - 48	17.476	0.246156	17.549	0.246535	16.8531	1083	783	6.26E+04	1.00E+03	3110	120	2.49E+07	7.00E+05	7.93	0.72
LR__42_RB_1 - 49	17.466	0.226189	17.539	0.226602	17.211	2457	1836	1.42E+05	2.40E+03	6560	200	5.65E+07	2.00E+06	1.98	0.75
LR__42_RB_1 - 50	240.369	3.05313	240.439	3.05313	17.8398	837	122.8	6.81E+05	3.90E+04	3.44E+04	1.90E+03	1.93E+07	1.40E+06	0.21	0.15
LR__42_RB_1 - 51	17.74	0.368267	17.813	0.368518	16.1688	228	127.1	13570	760	637	55	5.25E+06	3.20E+05	3.41	0.56
LR__42_RB_1 - 52	17.668	0.347298	17.741	0.347565	16.4464	425	284.7	24740	420	1199	72	9.78E+06	2.50E+05	5.62	0.66
LR__42_RB_1 - 53	18.027	0.266724	18.1	0.267074	16.8864	1096	983	6.51E+04	1.70E+03	3070	140	2.52E+07	1.10E+06	3.88	0.89
LR__42_RB_1 - 54	17.835	0.304021	17.908	0.304327	16.6416	654	466	3.79E+04	1.00E+03	1891	99	1.50E+07	4.60E+05	8.18	0.70
LR__42_RB_1 - 55	17.603	0.259904	17.676	0.260263	16.8701	1140	722	6.71E+04	1.50E+03	3130	140	2.62E+07	4.50E+05	3.65	0.63
LR__42_RB_1 - 56	17.726	0.443484	17.799	0.443691	16.2722	276.9	219	15350	540	761	80	6.36E+06	2.00E+05	5.35	0.78
LR__42_RB_1 - 57	17.502	0.298947	17.575	0.299259	16.7296	811	606	47430	950	2290	110	1.86E+07	5.70E+05	3.46	0.74
LR__42_RB_1 - 58	17.781	0.264914	17.854	0.265266	16.7322	839	443	4.91E+04	1.50E+03	2300	130	1.93E+07	3.40E+05	2.76	0.53
LR__42_RB_1 - 59	17.273	0.274639	17.346	0.274979	16.9842	1523	915	8.72E+04	3.70E+03	4070	200	3.50E+07	2.10E+06	0.81	0.59
LR__42_RB_1 - 60	18.437	0.410428	18.51	0.410652	16.3024	308	129	1.77E+04	3.00E+03	880	140	7.10E+06	1.30E+06	11.07	0.40
LR__42_RB_1 - 61	17.265	0.313928	17.338	0.314224	16.801	1019	521	57760	960	2620	110	2.34E+07	5.60E+05	-0.59	0.51
LR__42_RB_1 - 62	17.37	0.39491	17.443	0.395144	16.7177	715	948	40370	600	1830	110	1.64E+07	3.50E+05	0.06	1.32
LR__42_RB_1 - 63	17.835	0.331354	17.908	0.331634	16.6515	703	338	4.26E+04	2.70E+03	1910	140	1.61E+07	1.00E+06	-1.85	0.49
LR__42_RB_1 - 64	17.016	0.273015	17.089	0.273357	16.8038	999	700	5.59E+04	1.00E+03	2630	110	2.29E+07	7.80E+05	2.49	0.68
LR__42_RB_1 - 65	17.372	0.378503	17.445	0.378747	16.6126	636	424	37160	600	1830	150	1.46E+07	3.60E+05	6.45	0.66
LR__42_RB_1 - 66	18.199	0.287707	18.272	0.288031	16.4889	467	250	2.84E+04	1.20E+03	1455	97	1.07E+07	5.80E+05	8.53	0.54
LR__42_RB_1 - 67	18.031	0.376223	18.104	0.376469	16.5392	525	309	3.05E+04	3.00E+03	1490	180	1.21E+07	1.50E+06	3.26	0.57
LR__42_RB_1 - 68	17.554	0.259349	17.627	0.259709	16.8183	1014	645	6.01E+04	2.30E+03	2770	160	2.33E+07	1.20E+06	2.64	0.63
LR__42_RB_1 - 69	17.204	0.289579	17.277	0.2899	16.5742	605	310	3.36E+04	1.70E+03	1590	150	1.39E+07	6.40E+05	6.02	0.50
LR__42_RB_1 - 70	17.725	0.308852	17.798	0.309153	16.5376	516	376	30610	550	1371	79	1.18E+07	2.80E+05	-2.45	0.72
LR__42_RB_1 - 71	17.306	0.348746	17.379	0.349012	16.8238	1045.3	666.5	5.88E+04	1.30E+03	2830	110	2.40E+07	1.90E+05	3.67	0.64

Appendix 2
Zircon trace element analyses: background and data

Background for trace element analyses

Session	spot size	refernce material	masses measured (amu)	quality control refernce material	Internal Standard
Session 2021118_1b	30	NIST610	27, 28, 31, 49, 89, 91, 93, 138, 139, 140, 141, 146, 147, 153, 157, 159, 163, 165, 166, 169, 172, 175, 178, 181, 232, 238	91500, Synth Zircon Blank	Si, 15.2 wt%

Abbreviations

Ti (corr) ppm = Ti(measured in sample)/(average of Ti(measured in 91500))*4.73 (see details in Szymanowski et al., 2017)
Nb* = Nb(measured in sample) – (average Nb(measured in Synth Zirc Blank)
Eu/Eu* = (Eu/0.058)/(SQRT(Sm/0.153*Gd/0.2055))

Reference

Szymanowski, D., Wotzlaw, J.F., Ellis, B., Bachmann, O., Guillong, M., Quadt, A.V., 2017. Protracted near-solidus storage and pre-eruptive rejuvenation of large magma reservoirs. Nature Geoscience, **10**: 777–782.

Samples	Position	Th_corrected_Age	Th_corrected_Age_2SE	Al	La	Ce	Pr	Nd	Sm	Eu	Gd	Tb	Dy	Ho	Er	Tm	Yb	Lu	P	Ti (corr)	2SE Ti (corr)
LR__42_RB_1 - 2	rim	17.21	0.25	b.d.	b.d.	22.15	b.d.	1.419	3.59	0.742	23.82	8.98	124.2	49.61	254.9	58.3	546.4	114.3	484	3.39	0.35
LR__42_RB_1 - 6	rim	17.50	0.29	b.d.	b.d.	9.61	b.d.	0.575	1.18	0.279	7.85	3.059	48.09	20.9	116.6	29.92	310.7	72.5	270	3.48	0.41
LR__42_RB_1 - 11	rim	17.88	0.30	b.d.	0.0099	14.02	0.0918	1.67	4.36	1.089	32.1	12.74	189.8	80.9	421	97.3	908	186.5	525	6.79	0.66
LR__42_RB_1 - 12	rim	17.34	0.31	b.d.	0.0203	14.2	0.189	3.06	5.6	1.24	29.8	10.3	137	55	281	66.1	641	138	496	3.24	0.37
LR__42_RB_1 - 14	rim	17.60	0.28	b.d.	0.01	20.42	0.0576	0.966	2.54	0.595	15.67	5.65	80	32.13	169.4	40.96	415.6	90.3	345	2.93	0.38
LR__42_RB_1 - 15	rim	17.17	0.26	b.d.	b.d.	13.96	0.0258	0.492	1.632	0.267	12.69	5.46	84.9	37.95	210.4	52.9	541	120	333	2.13	0.22
LR__42_RB_1 - 18	rim	17.86	0.33	b.d.	0.0059	15.73	0.035	0.739	1.9	0.455	14.37	5.87	87.8	38.9	216	53.2	537	120.7	368	2.41	0.27
LR__42_RB_1 - 19	rim	17.40	0.31	b.d.	0.0116	19.21	0.052	1.013	3	0.586	22.77	9.23	130.9	54.1	275.6	64.2	594	125.9	493	2.18	0.28
LR__42_RB_1 - 20	rim	18.35	0.31	b.d.	0.0106	12.7	0.0443	0.79	1.74	0.493	12.3	4.81	73.4	31.1	172	41.8	418	93.8	368	4.89	0.61
LR__42_RB_1 - 25	rim	17.47	0.43	b.d.	0.0216	12.2	0.1	1.8	3.28	0.97	20.7	7.55	107.1	44.3	237	57.3	589	130	584	3.24	0.37
LR__42_RB_1 - 26	rim	17.36	0.29	b.d.	0.0074	13.77	0.0309	0.648	1.67	0.368	12.57	5.06	73.7	31.6	173	43.3	440	97.5	316	2.24	0.45
LR__42_RB_1 - 27	rim	17.84	0.38	b.d.	b.d.	10.31	0.0356	0.544	1.34	0.332	9.49	3.528	53.4	23.5	132.5	33.86	345.4	80.9	313	3.49	0.40
LR__42_RB_1 - 28	rim	17.93	0.31	b.d.	0.0083	15.23	0.0381	0.755	1.64	0.413	12.61	5.07	74.7	31.8	171.2	42.9	426	95.4	330	2.68	0.30
LR__42_RB_1 - 29	rim	17.42	0.40	b.d.	0.0083	13.01	0.0532	0.633	1.61	0.359	10.27	3.98	58.5	24.3	131.2	32.9	341	75.6	267	2.91	0.54
LR__42_RB_1 - 31	rim	17.22	0.35	b.d.	0.0082	13.27	0.0362	0.785	1.56	0.396	10.67	4.095	58.9	24.05	126.7	31.47	306.5	66.98	312	4.44	0.43
LR__42_RB_1 - 33	rim	17.60	0.29	b.d.	0.0131	10.81	0.132	1.97	4.17	0.834	20.99	7.2	97.8	38.82	194.7	46.6	460	100.9	261	2.60	0.27
LR__42_RB_1 - 37	rim	17.78	0.34	b.d.	0.0082	8.6	0.0262	0.409	1.032	0.231	6.01	2.343	34.36	14.71	81	21.1	218.4	50.48	244	2.93	0.39
LR__42_RB_1 - 40	rim	17.15	0.28	b.d.	b.d.	17.43	0.0637	1.227	2.95	0.615	20.83	8.49	127.2	54.6	290.2	70.2	675	144.3	504	3.40	0.32
LR__42_RB_1 - 44	rim of 43	17.74	0.29	b.d.	0.0061	13.62	0.0469	0.978	2.53	0.489	17.7	7.25	110	47	252.3	60	580	126.4	471	3.47	0.31
LR__42_RB_1 - 45	rim	17.91	0.30	b.d.	0.0075	11.93	0.0511	0.941	2.1	0.483	15.18	6	89.3	38.3	206.6	51.22	511.6	113.3	363	3.61	0.47
LR__42_RB_1 - 47	rim	17.47	0.25	b.d.	0.0085	20.41	0.0378	0.779	2.52	0.391	18.61	7.91	121.1	52.96	289	71.3	714	154.9	510	2.25	0.29
LR__42_RB_1 - 52	rim	17.74	0.35	b.d.	0.0085	9.39	0.0296	0.54	1.2	0.252	7.54	2.764	41.7	17.23	94.8	23.36	235.3	53.04	297	3.48	0.40
LR__42_RB_1 - 55	rim	17.68	0.26	b.d.	b.d.	20.04	0.0605	1.101	3.09	0.62	23.8	9.78	146.5	63.7	334.1	79.2	767	164.5	605	2.91	0.37
LR__42_RB_1 - 57	rim	17.58	0.30	b.d.	0.0088	16.56	0.0621	1.11	2.97	0.575	21.31	8.42	118.1	49.6	256.1	59.5	562.6	120.2	551	4.21	1.05
LR__42_RB_1 - 58	rim of 59	17.85	0.27	b.d.	0.0084	12.82	0.0408	0.638	1.79	0.371	14.14	5.79	85.1	37.36	196.4	48.3	478	105.5	393	2.04	0.36
LR__42_RB_1 - 65	rim	17.45	0.38	b.d.	b.d.	10.82	b.d.	0.626	1.28	0.348	9.39	3.53	51.2	21.6	116.9	29	286	66.8	348	2.30	0.49
LR__42_RB_1 - 68	rim	17.63	0.26	b.d.	b.d.	15.54	b.d.	0.741	2.05	0.416	15.21	6.27	93.7	40.3	220	53.7	535	119.9	460	2.58	0.28
LR__42_RB_1 - 70	rim	17.80	0.31	b.d.	0.0052	12.62	0.0433	0.629	1.529	0.355	9.7	3.574	50.8	21.4	115.1	28.69	296.2	67.3	382	4.20	0.33
LR__42_RB_1 - 71	rim	17.38	0.35	b.d.	0.0102	13.08	0.0296	0.552	1.577	0.282	11.67	4.581	67.4	28.48	149.8	36.42	360.1	78.8	386	1.54	0.22

Samples	Zr	Y	Nb*	Ba	Hf	Ta	Th	U	Eu/Eu*	Th/U	Yb/Dy	Zr/Hf
LR__42_RB_1 - 2	4.95E+05	1635	6.13	0.069	8930	2.389	961.0	1181.0	0.25	0.81	4.40	55.48
LR__42_RB_1 - 6	4.95E+05	750.3	2.13	b.d.	9400	1.26	203.0	444.0	0.28	0.46	6.46	52.67
LR__42_RB_1 - 11	4.87E+05	2725	4.93	0.095	8750	1.535	476.0	576.5	0.28	0.83	4.78	55.61
LR__42_RB_1 - 12	4.99E+05	1860	1.89	b.d.	9110	0.941	571.0	724.0	0.29	0.79	4.68	54.76
LR__42_RB_1 - 14	5.20E+05	1122	3.934	0.072	9870	2.034	1148.0	1180.0	0.29	0.97	5.20	52.68
LR__42_RB_1 - 15	4.99E+05	1330	5.91	0.07	10230	3.25	383.0	884.0	0.18	0.43	6.37	48.81
LR__42_RB_1 - 18	5.05E+05	1353	4.69	0.064	9800	2.186	460.0	867.0	0.27	0.53	6.12	51.53
LR__42_RB_1 - 19	4.91E+05	1782	7.39	0.063	9470	2.883	880.3	1273.0	0.22	0.69	4.54	51.89
LR__42_RB_1 - 20	4.95E+05	1120	2.97	0.063	8990	1.186	280.0	454.0	0.33	0.62	5.69	55.07
LR__42_RB_1 - 25	4.83E+05	1570	1.72	0.079	8250	0.869	483.0	620.0	0.36	0.78	5.50	58.57
LR__42_RB_1 - 26	5.30E+05	1099	3.84	0.076	10310	2.064	382.2	776.0	0.25	0.49	5.97	51.41
LR__42_RB_1 - 27	4.82E+05	850	2.123	0.071	8950	1.194	187.5	383.9	0.28	0.49	6.47	53.80
LR__42_RB_1 - 28	4.91E+05	1135	3.35	0.081	9570	1.434	483.0	687.0	0.28	0.70	5.70	51.35
LR__42_RB_1 - 29	5.14E+05	875	2.66	b.d.	10030	1.427	511.0	726.0	0.27	0.70	5.83	51.25
LR__42_RB_1 - 31	5.14E+05	846	2.053	b.d.	9580	1.17	522.0	601.0	0.30	0.87	5.20	53.65
LR__42_RB_1 - 33	5.01E+05	1312	1.11	0.055	9440	0.74	386.0	532.0	0.27	0.73	4.70	53.02
LR__42_RB_1 - 37	5.02E+05	510	1.176	0.063	10030	0.849	200.1	399.1	0.28	0.50	6.36	50.02
LR__42_RB_1 - 40	4.93E+05	1849	6.99	0.063	8920	2.418	480.3	907.0	0.24	0.53	5.31	55.31
LR__42_RB_1 - 44	4.97E+05	1576	5.57	b.d.	8940	1.913	307.5	638.0	0.22	0.48	5.27	55.60
LR__42_RB_1 - 45	4.92E+05	1329	4.293	0.085	8950	1.88	373.6	755.0	0.26	0.49	5.73	55.02
LR__42_RB_1 - 47	4.87E+05	1834	7.74	0.074	10010	3.669	600.4	1156.0	0.17	0.52	5.90	48.67
LR__42_RB_1 - 52	5.02E+05	602	1.336	0.066	9700	0.893	241.7	413.2	0.26	0.58	5.64	51.74
LR__42_RB_1 - 55	4.92E+05	2090	8.39	b.d.	9140	2.937	616.0	1097.0	0.22	0.56	5.24	53.82
LR__42_RB_1 - 57	4.86E+05	1647	6	b.d.	8820	2.049	526.5	795.0	0.22	0.66	4.76	55.07
LR__42_RB_1 - 58	4.99E+05	1273	4.53	0.079	9500	2.284	366.0	787.0	0.23	0.47	5.62	52.55
LR__42_RB_1 - 65	4.92E+05	760	2.11	b.d.	9620	1.27	356.3	604.0	0.31	0.59	5.59	51.19
LR__42_RB_1 - 68	4.88E+05	1396	5.66	0.077	9710	2.68	563.2	998.0	0.23	0.56	5.71	50.28
LR__42_RB_1 - 70	4.95E+05	749	2.09	b.d.	9490	1.206	327.7	510.5	0.28	0.64	5.83	52.12
LR__42_RB_1 - 71	4.95E+05	973	3.01	0.084	10440	2.046	574.0	1002.0	0.20	0.57	5.34	47.42

Appendix 3

Cathodoluminescence images of the separated zircon crystals from Bătrâni Tuff and the spots (30 μm) of analyses